On Consistent Parameterizations for Both Dominant Wind-Waves and Spectral Tail Directionality

Matias Alday, Fabrice Ardhuin

JGR Oceans

RESEARCH ARTICLE
10.1029/2022JC019581

On Consistent Parameterizations for Both Dominant Wind-Waves and Spectral Tail Directionality

Matias Alday[1,2] **and Fabrice Ardhuin**[2]

[1]Marine Renewable Energies Lab, Offshore Engineering Group, Department of Hydraulic Engineering, Delft University of Technology, Delft, The Netherlands, [2]Laboratoire d'Océanographie Physique et Spatiale, University Brest, CNRS, IFREMER, IRD, Brest, France

Key Points:

- A spectral wave model is adjusted to produce accurate properties for both dominant and short waves
- A balance between four-wave non-linear interactions and dissipation can explain directional bimodality
- Dissipation must be very weak for waves traveling at 90° and more from the wind direction

Correspondence to:

M. Alday,
M.F.AldayGonzalez@tudelft.nl;
malday@ifremer.fr

Citation:

Alday, M., & Ardhuin, F. (2023). On consistent parameterizations for both dominant wind-waves and spectral tail directionality. *Journal of Geophysical Research: Oceans*, *128*, e2022JC019581. https://doi.org/10.1029/2022JC019581

Received 14 DEC 2022
Accepted 30 MAR 2023

The copyright line for this article was changed on 3 OCT 2023 after original online publication.

Abstract Numerical wave models have been developed to reproduce the evolution of waves generated in all directions and over a wide range of wavelengths. The amount of wave energy in the different directions and wavelength is the result of a number of physical processes that are not well understood and that may not be represented in parameterizations. Models have generally been tuned to reproduce dominant wave properties: significant wave height, mean direction, dominant wavelengths. A recent update in wave dissipation parameterizations has shown that it can produce realistic energy levels and directional distribution for shorter waves too. Here, we show that this new formulation of the wave energy sink can reproduce the variability of measured infrasound power below a frequency of 2 Hz, associated with a large energy level of waves propagating perpendicular to the wind, for waves with frequencies up to 1 Hz. The details are sensitive to the balance between the non-linear transfer of energy away from the wind direction, and the influence of dominant and relatively long waves on the dissipation of shorter waves in other directions.

Plain Language Summary As the wind blows over the ocean, waves are generated in all directions and over a wide range of wavelengths. The amount of wave energy in the different directions and wavelength is the result of a number of physical processes that are not well understood. Practical models used for marine weather and engineering use a decomposition of the wave field across all these different directions and wavelengths. The sources and sinks of energy of the different components have usually been adjusted to properly represent the total energy, the dominant wavelengths, and mean directions, with generally bad results for the shorter wave energy and its directional distribution. Here, we show that a recently proposed formulation for the energy sink can be adapted to produce realistic levels of short wave energy in all directions, revealing the importance of different evolution time scales for different wave components. Our wave model is validated using a wide range of measurements, including underwater infrasound power that is related to the presence of waves in opposing directions.

1. Introduction

Parameterizations in numerical models are generally introduced to describe processes that cannot be explicitly represented because they are not fully understood or would require a computational power that is not available. For ocean and atmosphere circulation models, this is particularly the case for small scale processes related to sub-grid motions. In wave models, the sea state is described by the power spectral density of the surface elevation $E(f, \theta)$, distributed across frequency f and direction θ, and parameterizations are mostly used in the representation of the spectral evolution source term $S(f, \theta)$ on the right hand side of the wave energy balance equation (Komen et al., 1994). These parameterizations are necessary because of either poorly understood physical processes, in particular for the source term $S_{in}(f, \theta)$ that represents the generation of waves by the wind (Janssen, 1991; Miles, 1957) and the dissipation source term $S_{ds}(f, \theta)$ that accounts for wave breaking (Phillips, 1985), or processes for which the accurate theoretical source term takes a form that is too costly to evaluate at each model time step. The latter is the case of the non-linear four-wave interaction source term $S_{nl}(f, \theta)$ (Hasselmann, 1962), for which the discrete interaction approximation (DIA) of Hasselmann et al. (1985) is the parameterization used in most application cases. The DIA simplifies the interaction for each spectral component as the interaction within only two sets of four interacting wave components, known as quadruplets, instead of the integration over many more quadruplets, possibly thousands of them.

The general difficulty of wave modeling is that the model uses a spectral dissipation rate $S_{ds}(f, \theta)$ that is not measured directly. Here, we will particularly discuss the impact of the spectral shape of S_{ds} on the shape of the wave spectrum $E(f, \theta)$. Because full directional measurements are extremely rare (Guimarães et al., 2020), we generally have to work from the direction-integrated spectrum,

$$E(f) = \int_0^{2\pi} E(f,\theta)\mathrm{d}\theta, \tag{1}$$

and the directional distribution of wave energy,

$$M(f,\theta) = E(f,\theta)/E(f). \tag{2}$$

Wave buoys and other point measurement systems provide reliable estimates of the first five moments $E(f)$, $a_1(f)$, $b_1(f)$, $a_2(f)$, $b_2(f)$ (Ardhuin, Stopa, et al., 2019; Longuet-Higgins et al., 1963; Swail et al., 2009), with

$$a_n(f) = \int_0^{2\pi} \cos(n\theta)M(f,\theta)\mathrm{d}\theta, \quad b_n(f) = \int_0^{2\pi} \sin(n\theta)M(f,\theta)\mathrm{d}\theta. \tag{3}$$

From these moments, several frequency-dependent parameters can be derived from the spectrum to characterize the directional distribution. Besides mean directions, the directional spread $\sigma_1(f)$, as defined by Kuik et al. (1988), is reliably measured for frequencies up to 0.4 Hz (O'Reilly et al., 1996). A second spreading parameter $\sigma_{2,E}$ can give additional information and was extensively used by Ewans (1998) to establish that the wave spectrum is generally bimodal at high frequencies, as suggested by model simulations (Banner & Young, 1994). Here, we will use the alternative form $\sigma_2 = \sqrt{1-\sigma_{2,E}^2}$, which is denoted $\sigma^\star$ in Kuik et al. (1988). Hence, the two spreads have values in radians given by

$$\sigma_1(f) = \sqrt{2\left(1-\sqrt{a_1^2+b_1^2}\right)}, \quad \sigma_2(f) = \sqrt{0.5\left(1-\sqrt{a_2^2+b_2^2}\right)}. \tag{4}$$

Another parameter that is defined from $M(f, \theta)$ and has been much less studied because it is not accessible from buoy data is the so-called "overlap integral" $I(f)$,

$$I(f) = \int_0^{2\pi} M(f,\theta)M(f,\theta+\pi)\mathrm{d}\theta. \tag{5}$$

Indeed underwater acoustic measurements at frequencies $f_s = 2f$ with f in the range 0.1–10 Hz, are expected to be proportional to the value of $E(f)^2 I(f)$ (Ardhuin et al., 2013; Farrell & Munk, 2010), while $E(f)$ at those frequencies has a limited range of variation (Elfouhaily et al., 1997; Yurovskaya et al., 2013). Hence, underwater acoustics open a unique window on wave frequencies beyond 0.4 Hz s for which spectral information is very limited.

In the present paper, we particularly focus on the form of the dissipation term associated to wave breaking. Our starting point in Section 2 is a description of the parameterization proposed by Romero (2019), who introduced unique features that make it possible to reproduce the directional distribution of waves with frequencies higher than twice the wind sea peak frequency. We also present possible adjustments that may be needed to fit a wide range of observations. In Section 3, we look at the global-scale performance of this parameterization using usual satellite altimeter and buoy data that provide a measure of the dominant waves, and underwater acoustic measurements that give some control of the directionality in the spectrum tail. Discussions and conclusions follow in Section 4.

2. Dissipation Parameterization and Impact on Spectral Shape

At very high frequencies, the dissipation caused by molecular viscosity that scales like the wavenumber squared should be important, together with the straining of turbulence by the Stokes drift shear that scales like the wavenumber to the power 1.5 (Ardhuin & Jenkins, 2006). These are particularly relevant for gravity-capillary waves (Dulov & Kosnik, 2009), and certainly contribute to the shape of the full spectrum (Elfouhaily et al., 1997), with an indirect effect on the dominant waves via the wind stress (Janssen, 1991). However, as we limit our

investigation to a maximum frequency of 1 Hz, we will neglect these effects and the dissipation is expected to be controlled by wave breaking (Sutherland & Melville, 2013).

With very limited information on the distribution of wave energy as a function of wave direction θ, the first discussions of the spectral shape were done in terms of the direction-integrated spectrum $E(f)$. Phillips (1958) proposed that the non-dimensional spectrum $\alpha(f) = E(f)\ (2\pi)^4 f^5/g^2$ is constant at high frequencies, because in that range, all waves are breaking and thus have the same self-similar shape and the energy level "saturates." The main focus of the present paper is how we go back from a direction-integrated view of the spectrum to a full two-dimensional spectrum.

The idea of saturation was generalized to a two-dimensional spectrum by Phillips (1985) who proposed that the degree of saturation, which is a non-dimensional quantity,

$$B(k,\theta) = k^3 E(k,\theta) \tag{6}$$

determines the geometry of the surface and the form of the source terms. Hereinafter, we will use either wave frequency f or wavenumber k for the spectral dimension, exchanging one for the other using linear wave theory. In practice, we note that the wavenumber spectrum is less affected by non-linear effects than the frequency spectrum and may thus be preferred (Banner, 1990; Leckler et al., 2015). Phillips introduced the idea that the dissipation should be related to the length of breaking crests $\Lambda(k,\theta)$. Phillips (1985) proposed that, for a smooth enough spectrum, it is possible to use $B(k,\theta)$ as a measure of the steepness and parameterize $S_{ds}(k,\theta)$ as a function of $B(k,\theta)$. In measurements, it is much more difficult to define breaking probabilities and dissipation rates for different spectral components. Early measurements by Banner et al. (2000) focused on dominant waves and found that there is a threshold-like behavior for breaking probabilities as a function of a dominant wave steepness. The next step was to extend this to the frequency spectrum based on observations by Banner et al. (2002). The first attempts failed to produce a reasonable energy balance and spectral shape. In particular, the measurements suggested that short waves break more often in the presence of longer waves (Babanin & Young, 2005). This observation is very important and should be the topic of much more research. At present, a full theory for the modulation of wave breaking and associated dissipation rates of short waves is still missing and many different physical processes have been proposed to explain this behavior, leading to a wide range of parameterizations.

For example, Banner et al. (1989) observed that the passage of a breaking front with a phase speed vector $\mathbf{C}(\mathbf{k}')$ may "wipe out" all slower waves with a phase speed vector $\mathbf{C}(\mathbf{k})$. This effect was parameterized by Ardhuin et al. (2010), assuming that any breaking wave instantly dissipates a fraction $|C_{cu}|$ of the energy of all shorter waves provided that the short wave frequency is less than r_{cu} times the long wave frequency, giving a dissipation term

$$S_{ds,cu,-}(k,\theta) = C_{cu} N(k,\theta) \int_{k'<r_{cu}^2 k} \left|\mathbf{C}(\mathbf{k}) - \mathbf{C}(\mathbf{k}')\right| \Lambda(\mathbf{k}')\, d\mathbf{k}', \tag{7}$$

in which C_{cu} is a tuning factor of order -1, and we note that the dissipation rate is relatively higher for short waves traveling against the long breaking waves. This expression led to the first successful practical wave model based on a saturation dissipation that strongly reduced wave model errors and was implemented in most operational wave forecasting centers starting with Météo-France and NCEP in 2012, followed by Environnement Canada, the UK Met Office, and finally ECMWF as of June 2019.

However, these parameterizations are far from perfect. First of all, the typical balance of source terms led to a high frequency spectrum tail proportional to $f^{-4.5}$ and thus it still required an imposed parametric tail for the high frequencies. This parametric tail forces the spectrum to decay like f^{-5} from the spectral level at a frequency f_t set to be 2.5 times the windsea mean frequency. In practice, the parameterizations based on Ardhuin et al. (2010) produce energy levels at f_t, and thus for the entire tail, that is rather high for young waves and winds over 18 m/s. A high tail level produces a very high drag coefficient via the quasi-linear effect. Still the resulting energy balance produces wave heights that match observed wave heights up to at least 15 m (Alday et al., 2021; ECMWF, 2019).

On a practical side, the expression in Equation 7 involves a relatively costly integral because the norm of the phase velocity difference varies with the direction of the short and the long waves. This integral was left out in the ECMWF implementation. As an alternative, a good approximation is obtained by using the difference of the norms,

$$S_{\mathrm{ds,cu,+}}(k,\theta) = -C_{\mathrm{cu}} N(k,\theta) \int_{k'<r_{\mathrm{cu}}^2 k} \Big(|\mathbf{C}(\mathbf{k})| - \big|\mathbf{C}(\mathbf{k}')\big| \Big) \Lambda(\mathbf{k}') \mathrm{d}\mathbf{k}', \tag{8}$$

with C_{cu} a tuning factor of order 1.

2.1. The Parameterization by Romero (2019)

Romero (2019) started from recent observation of spectral shapes (Romero & Melville, 2010) breaking probabilities (Sutherland & Melville, 2015) and dissipation rates. He was the first to parameterize $\Lambda(\mathbf{k})$ as a function of the two-dimensional saturation $B(k, \theta)$ without any integration in frequency or direction,

$$\Lambda(\mathbf{k}) = \frac{l}{k} \exp\left(-\frac{B_{\mathbf{r}}}{B(\mathbf{k})} \right) M_L(\mathbf{k}) M_W(\mathbf{k}), \tag{9}$$

where $l = 3.5 \times 10^{-5}$ is a dimensionless constant and $B_r = 0.005$ is a threshold for the two-dimensional saturation spectrum, that is related to the threshold for wave breaking (Banner et al., 2000). The two multiplicative terms M_L and M_W that directly modulate the breaking probability are there to parameterize the "cumulative dissipation effect." The idea is that short waves are modulated by long waves, making the short waves steeper on the crests of the long waves and thus more likely to break. Donelan (2001) formulated that kind of effect using a "partially integrated mean square slope," for all waves longer than k,

$$\mathrm{mss}(k) = \int_0^{2\pi} \int_0^k k^2 E\big(k', \theta\big) \mathrm{d}k' \mathrm{d}\theta, \tag{10}$$

which gives the same effect for all short waves and long wave directions. The first term M_L in Equation 9 is similar to Donelan's dissipation as it uses mss(k) with an added cosine-squared directional dependency that could be loosely justified by the modulation theory of Peureux et al. (2021),

$$M_L(k,\theta) = \left[1 + 400 \sqrt{\mathrm{mss}(k)} \cos^2(\theta - \theta_m) \right]^{1.5}, \tag{11}$$

where θ_m is the energy-weighted mean wave direction for the entire wave spectrum, hence close to the direction at the peak frequency. A discussion of this particular choice is deferred to Section 4.

The second term, M_W is a function of the wind speed and was added to help the model reproduce the transition between the f^{-4} and f^{-5} regions of the wave spectrum, or $k^{-2.5}$ to k^{-3} when considering wavenumber spectra (Lenain & Melville, 2017; Long & Resio, 2007),

$$M_W(k) = (1 + D_W \max\{1, k/k_o\})/(1 + D_W) \tag{12}$$

where $k_o = g\left[3/(28u_\star)\right]^2$, with $u_\star$ being the friction velocity, corresponds to the scale at which the spectrum was observed to transition from $k^{-2.5}$ to k^{-3}. D_W is a dimensionless factor with recommended values of 0.9 when the DIA is used and 2 when exact nonlinear wave interactions are computed. We finally note that the dissipation source term $S_{\mathrm{ds}}(\mathbf{k})$ is taken to be proportional to $\Lambda(\mathbf{k})$ with a dissipation rate per unit breaking crest length that is a function of a direction-integrated saturation level $B(k)$ as defined by Romero et al. (2012).

$$b(k) = C_{ds}^{\mathrm{sat}} \left(\sqrt{B(k)} - \sqrt{B_T} \right)^{2.5} / g^2, \tag{13}$$

with $B_T = 0.0011$ a direction-integrated saturation threshold, giving the dissipation source term

$$S_{\mathrm{ds}}(k,\theta) = b(k) \frac{\Lambda(k,\theta) c^5}{g^2}. \tag{14}$$

Romero (2019) only replaced the breaking parameterization (including the cumulative part) of Ardhuin et al. (2010), keeping all other aspects, including the swell dissipation based on Ardhuin et al. (2009) and wind-wave generation that was adapted from Janssen (1991). The parameterization by Romero (2019) can therefore be chosen in the WAVEWATCH III model by using the "ST4" option for S_{in} and S_{ds} parameterizations and only changing the value of a few model parameters, as listed in Table 1. The simulations using the original form of

Table 1
Choices of Parameterizations, Methods and Parameter Adjustments for the Different Models That Use the "ST4" Switch in WAVEWATCH III Version 7

Run:	Default	$C_{cu} = 0.3$	700	702	704	700-WRT	702-WRT	702-GQM	707-GQM
S_{nl}	DIA	DIA	DIA	DIA	DIA	WRT	WRT	GQM	GQM
n_B	1	1	3	3	3	3	3	3	3
C_{ds}			−3.8	−3.8	−3.8	−3.8	−3.8	−3.8	−2.3
C_{cu}	−0.4	0.3	0	0.3	0.3	0	0.3	0.3	0.35
r_{cu}	0.5	0.5	N.A.	0.5	0.5	N.A.	0.5	0.5	0.5
D_W	N.A.	N.A.	0.9	0	0.9	2.0	0.0	0.0	2.0
C_t	0.0	0.0	0.0	1.0	1.0	0.0	1.0	1.0	1.0
s_u	0.3	0.2	0.3	0.2	0.0	0.3	0.0	0.0	0.0

Note. The choice $n_B = 1$ corresponds to the choice of saturation definition given by Ardhuin et al. (2010), while $n_B = 3$ uses the local saturation defined by Romero (2019). C_{ds} is the first term on the RHS of Equation (13). When $C_{cu} < 0$ Equation (7) is used, when $C_{cu} > 0$ Equation (8). s_u is the sheltering coefficient from Ardhuin et al. (2009) used to tune the stress at high winds.

Romero's dissipation are given the identification number "700" in the following, but we have modified a few of the wind-wave generation parameters from those used by Romero (2019). Namely, the wind-wave growth parameter was generally increased from its value $\beta_{max} = 1.43$, and its maximum roughness length of 0.0008 m was deactivated.

In some calculations, we also added a dissipation term representing wave–turbulence interactions (Ardhuin & Jenkins, 2006), with the coefficient $C_t = 1$ corresponding to a constant momentum flux with depth, while Kantha (2006) argued that typically $C_t \simeq 0.5$. This extra term was found to have no significant impact on the tail part of the spectrum, but $C_t = 1$ may reduce developed wave heights by about 5% as it plays a relatively more important role in the energy balance at frequencies below that of the windsea peak.

We now illustrate the effects of source term parameterizations on simulated waves in a very simple idealized situation, representing a spatially uniform ocean starting from rest with constant 10 m/s wind. Because Romero adjusted all parameters to reproduce the growth of wave heights given by the ST4-default parameterization (Ardhuin et al., 2010), there is little difference in wave heights, as shown in Figure 1a. The interesting results brought by the T700 parameterization is that it can produce a shape of the spectrum tail that is close to a f^{-5} shape, for frequencies above 0.6 Hz (Figure 1b). Still the energy level is higher than the 0.7×10^{-3} m^2/Hz^4 reported by Leckler et al. (2015) for similar wind speeds but for younger waves. In the case of the standard ST4 and ST6, that shape was imposed above a frequency f_t that is a constant times the mean frequency of the windsea, applying the same directional distribution $M(f, \theta)$ for all f above f_t. This imposed tail is one of the reasons why the ratio of cross-wind (mssc) to down-wind (mssd) mean square slopes is much lower compared to T700, as shown in Figure 1c. We note that these slope variances are only integrated up to 1 Hz (1.5 m wavelength), and we have added the contribution of waves with $f > 1$ Hz, using Elfouhaily et al. (1997). Because 70% of the slope variance is carried by waves shorter than 1.5 m, and the Elfouhaily et al. (1997) spectrum is poorly constrained at wavelengths from 0.2 to 3 m, a direct comparison with observed ratios MSSC/MSSD is a little premature and will not be pursued here. An alternative validation performed by Romero and Lubana (2022) uses measured slope variance in the presence of oil slicks (C. Cox & Munk, 1954) but is only qualitative because the effect of the slick on the shape of the wave spectrum is not exactly known.

A more dramatic difference is found for the overlap integral $I(f)$. As noted by Romero and Lubana (2022), $I(f)$ given by T700 can be more than 10 times the value given by any other parameterization, with values around 0.1 for frequencies above 3 times the windsea peak frequency, consistent with stereo-video data (Leckler et al., 2015; Peureux et al., 2018). An interesting property is that the second-order wave field at large wavelengths has a power spectrum density at frequency $f_s = 2f$ that is proportional to $E^2(f)I(f)$. These components generate acoustic-gravity modes (C. S. Cox & Jacobs, 1989), seismic modes (Hasselmann, 1963) and microbaroms (Brekhovskikh et al., 1973), as reviewed by Ardhuin, Gualtieri, and Stutzmann (2019) and De Carlo et al. (2020). As a result, any underwater acoustic or seismic measurements at frequency $2f$ will be proportional to $E^2(f)I(f)$ (Duennebier

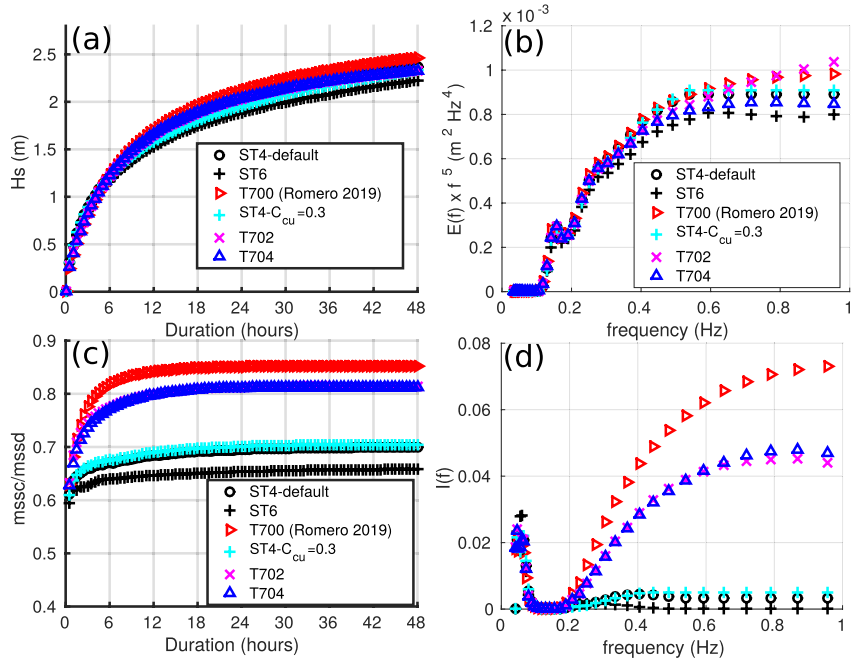

Figure 1. Time evolution of (a) wave height and (c) ratio of cross-wind over down-wind mean square slopes, and frequency distributions of (b) saturation level and (d) overlap integral after 30 h. Results with existing parameterizations based on ST4 (Ardhuin et al., 2010) and ST6 (Rogers et al., 2010) are shown for reference, together with Romero (2019) and several proposed adjustments (see Table 1).

et al., 2012; Farrell & Munk, 2008; Peureux et al., 2018), with the proportionality coefficient varying with depth and local sediment properties (Ardhuin et al., 2013). A factor 10 difference between modeled seismic response and data can be largely due to uncertainties in the seismic mode generation and dissipation (Ardhuin et al., 2013), but we expect that these effects are linear and only a function of location and frequency. Therefore, the observed temporal variation of underwater acoustic data should clearly discriminate between different parameterizations, as we shall see in Section 3.

In order to further improve on the parameterizations it is interesting to expose the features that give this spectrum behavior, namely the proper leveling of the direction-integrated saturation level $f^5E(f)$ and the directional broadening that gives these high $I(f)$ values. A distinctive feature of Romero (2019)'s parameterization is that both the dissipation term and the cumulative effect are highly directional. Thus, for directions more than 90° away from the wind, if the value of $B(k, \theta)$ is not high enough there is no dissipation at all, and since the wind input is zero (or weakly negative) the only source of energy for these very oblique waves is the non-linear energy flux. As a result, whatever little flux of energy comes from S_{nl} can accumulate to a significant energy level. Figure 2 shows the inverse dissipation time scales S_{ds}/E and the resulting directional spectra distribution at frequencies 0.5 and 1 Hz.

The first striking feature is that the previous parameterizations have a nearly isotropic S_{ds}/E. The use of a partial directional integration of $B(k, \theta)$ in the ST4-default of Ardhuin et al. (2010) gives a slightly larger dissipation in the wind direction compared to 30° away from the wind, but the dissipation remains relatively high for waves against the wind. In contrast, the relative dissipation S_{ds}/E from Romero (2019) goes to zero for wave directions 180–360°, allowing the spectrum to grow "broad shoulders" with high energy levels for directions 60–120 away from the wind, and still zero in the direction opposite to the wind. We note that a minor change in the cumulative term using Equation (8) with $S_{cu} = 0.3$ instead of Equation (7) slightly increases the width of the ST4-default spectra (cyan "+" symbols in Figures 1 and 2). But this effect is weak, and the dissipation rate is still high for the large oblique angles relative to the wind. We may combine this cumulative effect with the one used by Romero (2019) to get some control over the magnitude of the "broad shoulders." Here, we have proposed two versions of the parameterization. In T702 Romero's cumulative term is simplified by removing the wind dependent part and the isotropic cumulative term of Equation (8) is added with $S_{cu} = 0.3$. This gives almost the same direction-integrated spectrum at high frequencies, as shown in Figure 1b, but a much lower overlap due to

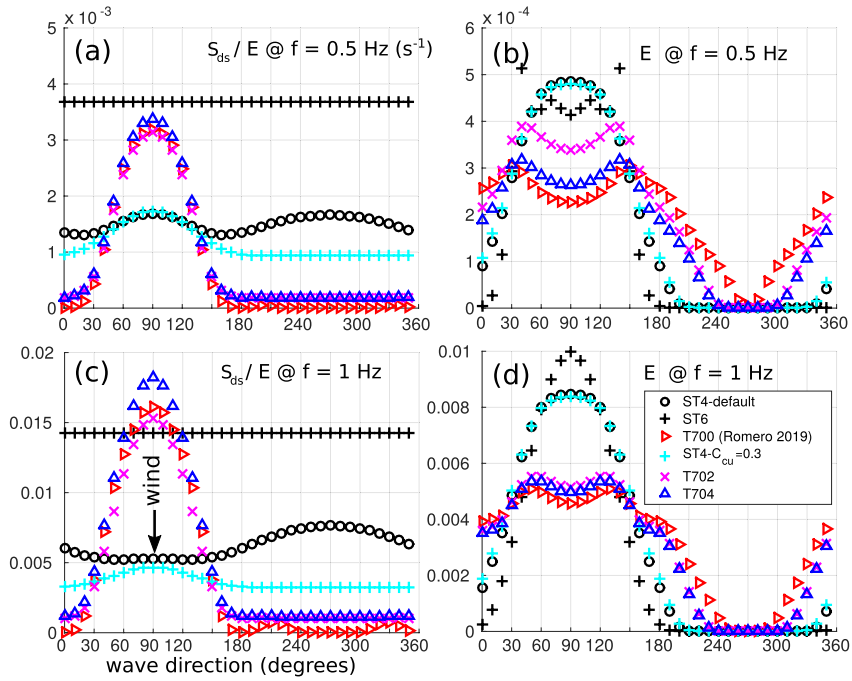

Figure 2. Inverse dissipation time scale S_{ds}/E and directional spectrum shape $E(f, \theta)$ for frequencies 0.5 and 1 Hz. These are obtained after 30 h of simulation for a uniform ocean with a constant wind speed of 10 m/s blowing in direction 90°.

the finite dissipation time scales (5,000 s at 0.5 Hz, 1,000 s at 1 Hz). Alternatively, the T704 parameterization combines both cumulative effects, in which case the wind sheltering can be removed ($s_u = 0$) and a good high frequency tail level can be obtained, very similar to the default ST4 parameterization and the typical observed saturation level (Leckler et al., 2015).

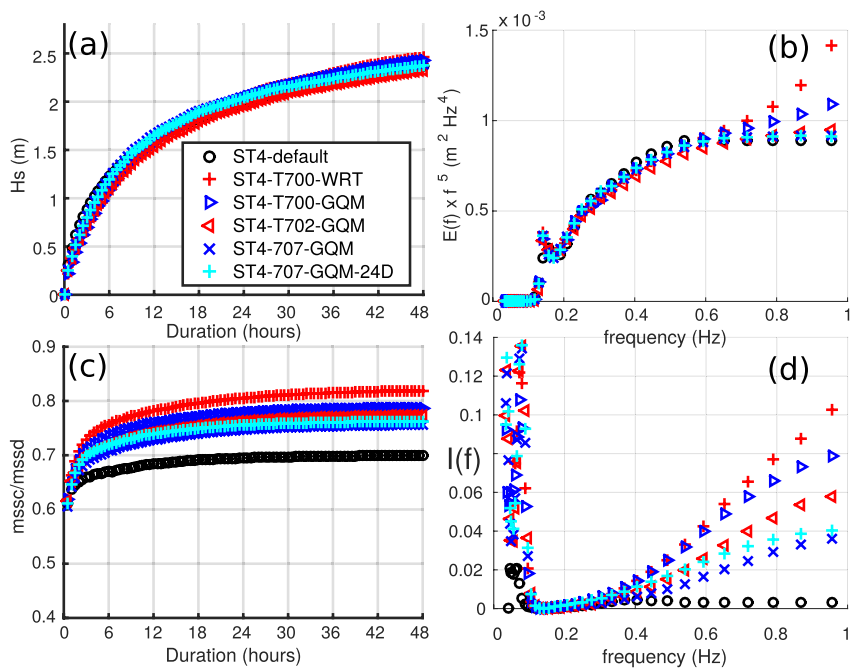

Figure 3. Same as Figure 1, for simulations using exact methods for the non-linear four-wave interactions.

Because the DIA is a poor approximation of the full non-linear interaction, it is interesting to check on the effect of using the full interaction which is computed here using two methods (Figures 3 and 4): Either the method of Webb (1978) and Tracy and Resio (1982) (hereinafter WRT) as implemented by van Vledder (2006), or the Gaussian Quadrature Method (GQM) of Lavrenov (2001), as implemented by Michel Benoit and optimized by Gagnaire-Renou et al. (2010). The GQM method relies on a change of variables for the resonant interactions that contribute to the source term $S_{nl}(f, \theta)$, for components (f, θ) interacting with (f_1, θ_1), (f_2, θ_2), and (f_3, θ_3), and transform to an integral over three dimensions that are f_1/f, θ_1, and $f_2/(f + f_1)$. Results shown here for GQM employ a coarse integration discretization using 11, 6, and 6 points along the three resonant integration dimensions, and we verified that the finer resolutions only enhanced the peaks in frequency and directional space by about 10%. Following Gagnaire-Renou (2010) we also filter out quadruplets with coupling coefficients lower than 0.05 times the maximum, and we have also filtered out quadruplets at frequencies for which $f^5E(f) < 5 \times 10^{-5}$ m^{2}s^{-4}. We note that each of these two filtering steps typically reduced the computation time by a factor 2, with no visible impact on the spectral shape. The only adjustment made to the other parameters follows the recommendation of Romero (2019) with the wind modulation coefficient D_w in Equation (12) changed from 0.9 to 2. This increased value of D_w was not sufficient to obtain a correct energy balance at high frequency, hence we also proposed a T707 adjustment that uses a reduced dissipation coefficient C_{ds} in Equation (13), similar to what is usually done when replacing the DIA method with exact interactions (Banner & Young, 1994), and we kept the wind sheltering coefficient at zero, as in the T704 adjustment with the DIA. We also note that model results with directional discretizations using 36 directions or 24 directions give very similar result, which is interesting for practical applications since the GQM, and the model in general, is faster when using 24 directions as we have chosen to use in Section 3.

Among all the runs obtained with exact interaction methods the only one that stands out with largest cross-wind slopes and overlap integrals is "ST4-T700-WRT," obtained without the isotropic cumulative effect of long wave breaking wiping out the shorter waves. Whereas ST4-T700-GQM is supposed to compute the exact same thing we note that the higher frequencies differ slightly with a higher energy level and larger cross-wind energy when the WRT method is used. By changing the number of model frequencies, and changing the maximum model discrete frequency f_{max} we have found that the WRT method as implemented often develops a spurious tail level for $f > 0.7f_{max}$. This effect is much less pronounced with the GQM implementation.

In order to understand the qualitative difference between DIA and exact calculations, it is useful to look at the energy balance as a function of direction, and in particular the relative dissipation rate S/E, shown in Figure 4. Contrary to the case with the DIA, the full interactions are able to fill all directions with some energy, including directions opposite to the wind, in particular at high frequencies, a phenomenon that has long been observed with High-Frequency (HF) coastal radars (Crombie et al., 1978). This effect was first modeled by Lavrenov and Ocampo-Torres (1999) in simulations without dissipation. The 17 dB difference between upwind and downwind energy levels for 0.5 Hz is compatible with the typical 20 dB difference in energy levels for wave upwind and downwind as recorded by 25 MHz HF radars (Kirincich, 2016). At 1 Hz, corresponding to $k = 4$ rad/m, the smaller difference with the T700-WRT simulation between upwind and downwind energy levels is a little surprising but no coastal radar data is available to probe these frequencies, and the stereo-video data reported by Peureux et al. (2018) in similar conditions are not conclusive due to a noise level of $E(k, \theta)$ that is probably obscuring the low energy level of waves opposing the wind. Other parameters like the lobe separation and lobe ratio (ratio energy in peak direction to energy in the wind direction) are overestimated at 1 Hz by ST4-T700-WRT. Using an extended model frequency range up to 1.5 Hz (not shown here) we found that the tail level and lobe ratio at 1 Hz is reduced and identical to the one obtained with ST4-T700-GQM, hence the higher lobe ratio with WRT appears to be an artifact of the treatment of the unresolved high frequencies. We find that the overlap integral is probably underestimated by the T707 parameterization, compared to the stereo-video data reported by Peureux et al. (2018). We also note that the high level of upwind energy at 1 Hz is large with T700-GQM and reduced by a factor 2 with 702-GQM which has a dissipation time scale of 600 s for upwind waves compared to 50 s for downwind waves (Figures 4c and 4d). One way to keep some of the general behavior of the source terms when also using a cumulative dissipation term given by Equation (8) is to make sure that it only acts at high enough frequencies, for example, with $r_{cu} > 2.5$. Further investigation of measured spectra in steady or turning winds can probably be used for additional testing of the parameterizations.

We also note that the two directional spreads that can be measured by directional buoys have different behaviors from narrow bimodal spectra to broad bimodal spectra as shown in Figures 4e and 4f. Indeed the σ_1 spread is

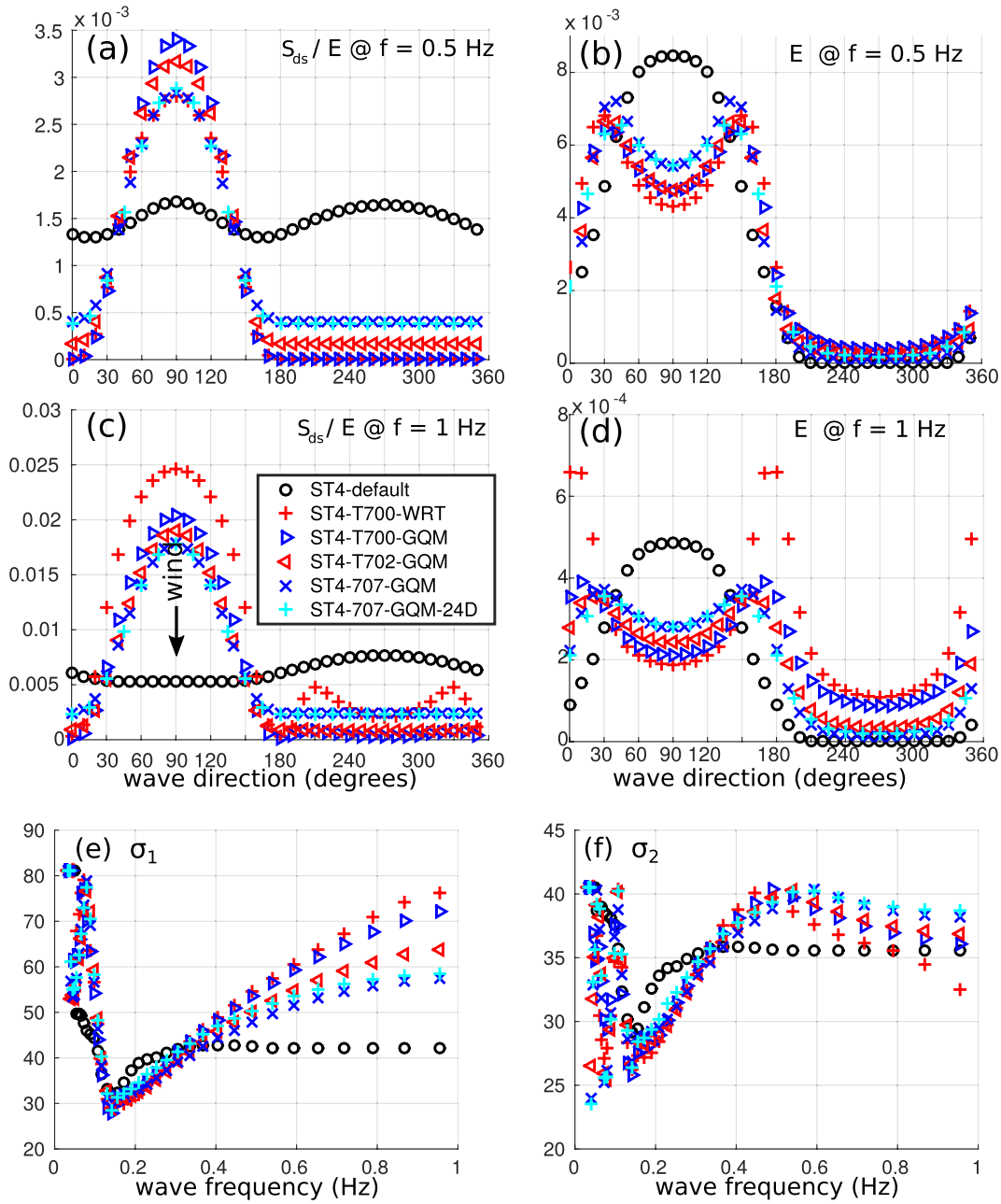

Figure 4. Same as Figure 2, for simulations using exact methods for the non-linear four-wave interactions, with the addition of directional spreads σ_1, defined from a_1 and b_1 directional moments, and σ_2, defined from a_2 and b_2 directional moments following Kuik et al. (1988).

defined from the a_1 and b_1 directional moments, and is maximum when the same amount of energy is found in opposite directions (i.e., when both a_1 and b_1 are zero). In constrast, σ_2, which is called $\sigma^\star$ by Kuik et al. (1988), is maximum when both a_2 and b_2 are zero which happens when the same amount of energy is found in perpendicular directions. Hence, σ_2 peaks at frequencies around 0.5 Hz where the two lobes are almost perpendicular and decreases towards higher frequencies as the lobes spread further apart, so that σ_1 keeps increasing toward higher frequency when σ_2 decreases. This behavior is very well described by Ewans (1998). Remember that Ewans (1998) uses $\sigma_{2,E} = \sqrt{1-\sigma_2^2}$ as discussed in the introduction, so that $\sigma_{2,E}$ and σ_2 are anti-correlated. For $f = 0.6$ Hz $= 4f_p$ in Figure 4, the typical values given by Ewans (1998) correspond to $\sigma_1 = 60°$ and $\sigma_2 = 37°$, which is closer to the T700-WRT and T700-GQM simulations.

3. Validations at Global Scale

We evaluate the parameterizations described above at the global scale. Our model configuration uses a regular grid in latitude and longitude with a 0.5° step, extending from 78° south to 80° north. We used a spectral grid with 24 directions and 36 frequencies. Frequencies are exponentially spaced from 0.034 to 1 Hz, with a constant ratio of 1.1 from one frequency to the next. Besides hourly winds from the fifth European Reanalysis ERA5 (Hersbach et al., 2020), the model uses daily sea ice concentration and the monthly iceberg mask from Ifremer CERSAT, and daily surface currents from Mercator-Ocean reanalysis GLORYS.

3.1. Wave Heights

As demonstrated by Ardhuin et al. (2010), wave heights from global-scale wave models are most sensitive to parameters defining the swell dissipation, and any change to the wave breaking dissipation can have an impact on the wind-sea to swell transition and thus on the energy radiated into swell. We thus repeated the parameter adjustment procedure defined by Alday et al. (2021), using the distribution of wave heights measured by Jason-2 for the year 2011, as provided in the ESA Sea State Climate Change Initiative version 1 dataset (Dodet et al., 2022). We recall that, following Leckler et al. (2013), we parameterize swell dissipation due to air-sea friction (Ardhuin et al., 2009) as a combination of viscous and turbulent terms with a transition at a Reynolds wavenumber Re_c spread out over a range of values s_7, in order to represent a Rayleigh distribution of wave heights (Perignon et al., 2014; Stopa et al., 2016). We ran the model with either T702 and the DIA or T707 and the GQM method. Both model runs are compared to the T475 which differs from the default ST4 by a small adjustment on the swell dissipation parameters (Alday et al., 2021). Here, the value of s_7 was reduced from 432,000 for T475 and T707-GQM to 360,000 for T702, and the swell dissipation factor was reduced from 0.66 for T475 and T707-GQM to 0.6 for T702. We also note that T475 and T702 use a wind-wave growth parameter $\beta_{\max} = 1.7$ while T707-GQM uses $\beta_{\max} = 1.6$, which is consistent with the general reduction of other source terms when replacing the DIA with an exact method (Banner & Young, 1994). These adjustments were performed for the year 2011.

We will now verify model results using independent data for the year 2007 that combines four different altimeters (GFO, Envisat, ERS-2 and Jason-1) provided in the ESA Sea State Climate Change Initiative version 1 dataset (Dodet et al., 2022). We also note that any adjustment is specific to the properties of the wind forcing. As mentioned above, we use winds from ERA5, which is known to have some regional biases (Belmonte Rivas & Stoffelen, 2019). To our knowledge this is the first publication discussing a global-scale 1-year long simulation using an exact calculation of 4-wave interactions. We used the "coarse" GQM integration settings proposed in Gagnaire-Renou (2010) and used in Beyramzadeh and Siadatmousavi (2022), with the same filtering details described in Section 2.1: a first filtering on the coupling coefficient that removes half of the quadruplets (leaving around 800 quadruplets for each spectral component, compared to 2 for the DIA) and a second filtering based on the value of $E(f)f^5$, so that on average the S_{nl} term is not computed for half of the spectral components, typically for the low frequency swells. We verified at a few buoy locations in the Pacific that this second filtering had a minor impact on the low frequency energy levels, which was typically reduced by under 5% for frequencies under 0.06 Hz. The CPU time was 7.5 times longer for the full model using GQM with 24 direction discretization compared to the DIA with 36 direction, taking 45 h of run time for 1 year of simulation, using 432 computational nodes. We note that a typical 6-day global forecast would typically take only 1 hr with the same set-up.

Wave heights in simulations with T702 and T707-GQM dissipation parameterization are very close to those obtained with T475. For wave heights, the mean difference is within ±2% locally (Figures 5b and 5c), with some stronger negative biases in the tropical west Pacific when using the new parameterizations. Random differences are also similar, with the Hanna-Heinold scatter index (Mentaschi et al., 2013) increasing from 6% in the trade wind areas to 15% and more along East coasts and in enclosed seas (Figures 5d–5f). We note that the random error of denoised 1 Hz altimeter measurements is of the order of 7% for the data used here (Dodet et al., 2022). We thus expect that in the trade wind areas most of the difference between model and satellite data is caused by random errors in satellite data. Typically the T707-GQM run gives a lower random differences than T475 in the Pacific, but larger values in the South Atlantic, and they have similar area-weighted averaged HH index of 10.4% for T475% and 10.3% for T707-GQM, compared to 10.6% for T702.

Although these differences are small, some systematic deviations are revealed when data points are gathered for a given measured H_s, as presented in Figure 6 for the same year 2007. Simulations with T702 and T700-GQM

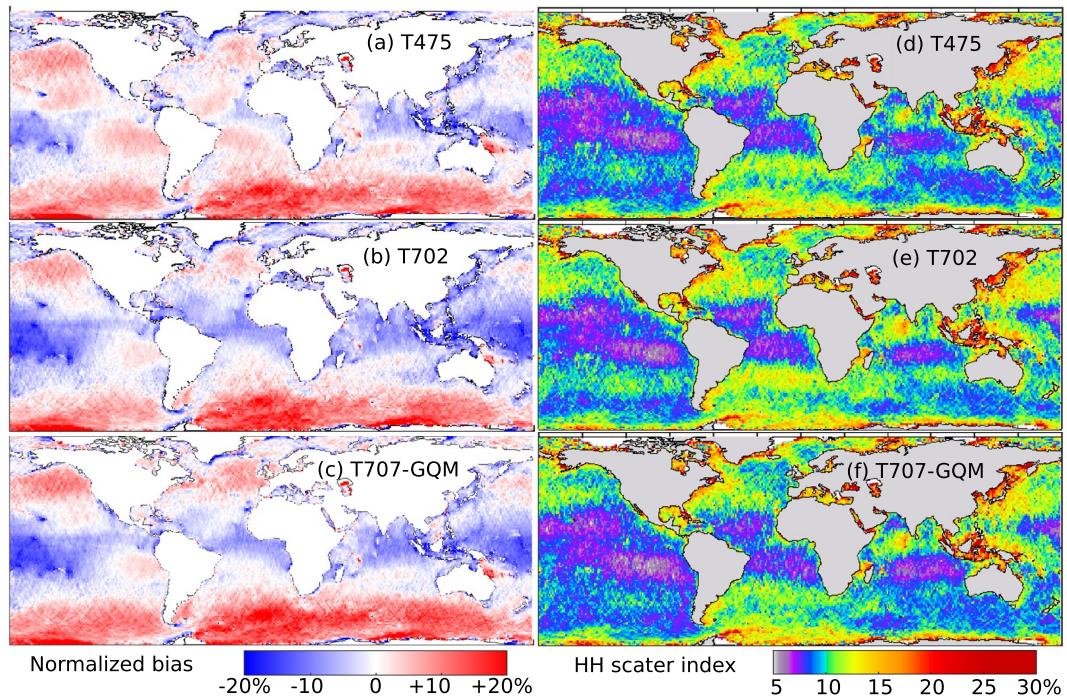

Figure 5. (a, b, c) Normalized mean difference in significant wave height between model runs and satellite altimeters for the entire year 2007 and (c, d, e) the Hanna-Heinold scatter index as defined by Mentaschi et al. (2013).

have a reduced bias compared to T475 for wave heights in the range 1–3 m, but present a higher scatter around the observed values. We suspect that most of these differences may be associated to swell dissipation.

For very large wave heights altimeters are usually most accurate, and they are consistent with other data up to 20 m wave height (Hanafin et al., 2012). Wave heights over 10 m account for 0.06% of the full altimeter record, but they are hugely important in defining extremes both locally and remotely through the radiation of swells (Hoeke et al., 2013). In that range of wave heights, the T700-GQM using most parameter values from Romero (2019) gave low biases from −10% to −15%, this is why we preferred to show the adjusted T707-GQM. We note that Romero (2019) also included a maximum air-side roughness of 0.0008 m which further reduces the wave heights for $H_s > 8$ m. This and other possible adjustment strategies are discussed in Section 4.

Examination of a few cases suggest that the T475 and T702 runs give tail levels much higher than T700-GQM for the high winds found in these cases, contrary to what was shown for 10 m/s winds in the previous section. We also recall that the wind input parameterization of Janssen (1991) assumes a tail decreasing like f^{-5} even in the capillary wave region, and does not even correct the dispersion relation for surface tension effects.

We may thus consider the T475 and T702 runs to be somewhat "lucky" in providing probably wrong spectral level and wind-wave growth term that leads to a correct growth of wave heights for $H_s > 10$ m. Efforts to resolve this are underway, and various observations of the spectral tail level and its variability (Yurovskaya et al., 2013) associated with remote sensing data (Ryabkova et al., 2019) and recent findings by Janssen and Bidlot (2023) may lead to more realistic spectra and wind stress. In this context, characterized by very few detailed spectral wave measurements, underwater acoustic data may provide interesting constraints on the source terms. In the following section we use data acquired in the deep ocean north of Hawaii by Duennebier et al. (2012), which covers wind speeds up to 17 m/s.

3.2. Underwater Acoustic Data and Directional Spectral Tail Properties

Recent model developments show that one could predict the variability of the seismic or acoustic wave energy at acoustic frequencies f_s in the range 0.08–0.4 Hz using a wave model like WAVEWATCH III. However, underwater acoustic data show that wave-induced signal extend all the way to 60 Hz (Duennebier et al., 2012; Farrell &

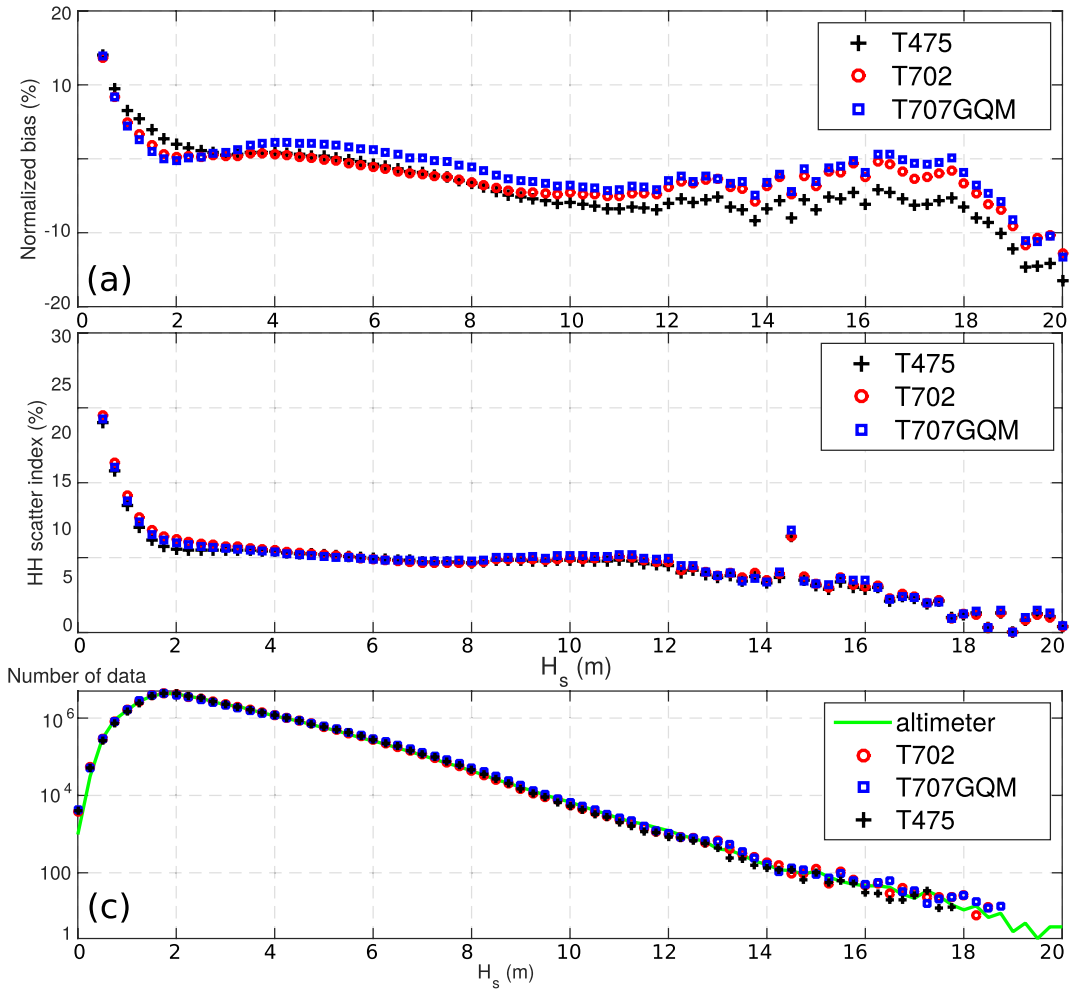

Figure 6. Model global performance with different parameterizations as a function of the wave height: T475, T702, and T707-GQM. Wave heights performance parameters for year 2011 (WW3—Jason-2). (a)H_s NMD and (b) HH scatter index.

Munk, 2010). Ardhuin et al. (2013) suspected that the poor acoustic model performance for $f_s > 0.4$ Hz was caused by an unrealistic directional wave spectra shape. This question was also discussed by Peureux and Ardhuin (2016) who proposed parameterizations of the directional distribution that could explain the observed acoustic levels.

One general difficulty of using seismic or acoustic data generated by the double-frequency mechanism of Longuet-Higgins (1950) and Hasselmann (1963) is that the absolute magnitude of the signal is influenced by bottom properties, as already noted by Abramovici (1968). Also, at the lower frequencies, typically $f_s < 0.3$ Hz, the signal can propagate over thousands of kilometers along the wave guide that is constituted by the water layer and the upper crust and sediment layers. As a result, it is not straightforward to link the local wave properties and the local acoustic field. However, for the higher frequencies, as the scale over which the signal is attenuated becomes shorter than the scale at which we can consider the sea state to be homogeneous, there should be a linear relation between the local value of $E^2(f)I(f)$ and the local seismic or acoustic power.

Farrell and Munk (2010) have analyzed ocean bottom hydrophone data in 5,000 m depth and showed that the acoustic level for frequencies 1–6 Hz transitions from a saturated level when the wind is above 5–6 m/s to a "bust" very low level when the wind drops below this value. This is expected to be caused by a narrowing of the spectrum as the wind sea peak frequency goes down closer to 0.2–0.5 Hz, and thus a very strong reduction of the overlap integral $I(f_s)$, by a factor at least 10. Because most parameterizations, including T475, use a diagnostic tail that made $M(f, \theta)$ constant above some frequency f_t, the value of $I(f)$ is frequency-independent above f_t and has a narrow range of variation. Romero and Lubana (2022) showed that T700 gave a much higher value of the overlap integral but did not directly compare predicted acoustic or seismic data to measurements.

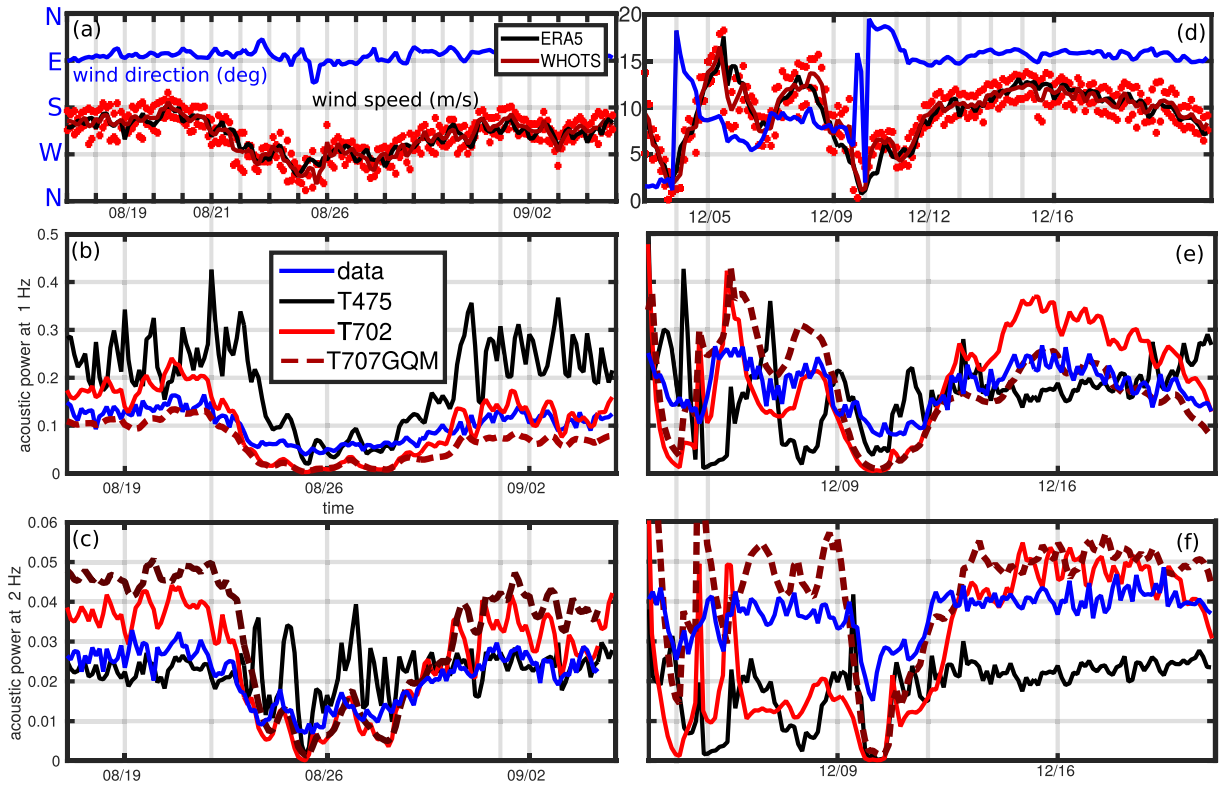

Figure 7. Time series of 3-hourly wind speed and direction and 10-min averaged measurements (panels a, d) and noise level over a few weeks of summer (a, b, c) and winter (d, e, f) in 2007 at the ALOHA Cabled Observatory, north of Ohahu Hawaii, using data provided by (Duennebier et al., 2012) and model runs T475, T700 and T700-GQM. In order to give results comparable to T700, results for T475 are multiplied by 10 for 1 Hz and 15 for 2 Hz.

Here we use data from the ALOHA cabled observatory provided by Duennebier et al. (2012), and compare the relative variation of local predicted seismo-acoustic source proportional to $E^2(f)I(f)$ with the ocean bottom acoustic power. The employed data corresponds to acoustic power spectra from 26 February to 31 December 2007. From the original spectra computed every 5 min, we take the spectral density that is lowest in a 3 h window and compare it to the time-centered model snapshot computed from the local wave spectrum. Choosing the minimum instead of a median mitigates the contribution of non-continuous noise sources, and generally gives a better correlation with the model.

Figure 7 shows time series of modeled seismic source time series and observed acoustic power for two typical time intervals with moderate (Easterly) trade winds in the summer, and a winter Southerly storm followed by intense trade winds. Note that the modeled acoustic noise was re-scaled because of the poorly known bottom amplification effect, with a larger re-scaling coefficient for T475. Farrell and Munk (2010) showed that the 2 Hz acoustic signal has a fairly constant level, here around 0.04 Pa^2/Hz (Figures 7c and 7f), with some occasional drops, which they called "busts." Such busts occur in our record when the wind speed decreases below 8 m/s, from 21 August to first of September and from 9 December to 12 December. This behavior is associated with 1 Hz surface gravity waves and is generally well reproduced by T702 and T707-GQM but not by T475, which has too narrow a range of variation of the seismo-acoustic source. The rise in modeled acoustic level is delayed with T707-GQM with a saturation that is only reached when the wind speed rises to 10 m/s and the general sensitivity of the modeled acoustic level is larger with T702 and T707-GQM, with an amplification by a factor 40 from a wind speed increase of 2 m/s to 10 m/s. While it is possible that background noise may obscure low noise levels, the analysis of Duennebier et al. (2012) suggests only a factor 10 increase for such a wind speed increase, while Farrell and Munk (2013) give a factor up to 30 (15 dB).

The behavior at 1 Hz is more complex, and there is no simple saturation of the acoustic energy in that case, but rather a general increase of acoustic power with increasing wind speed, which in this case is exaggerated by T700 and not well followed by T475 when the wind speed exceeds 10 m/s. The model with T702 and T707-GQM

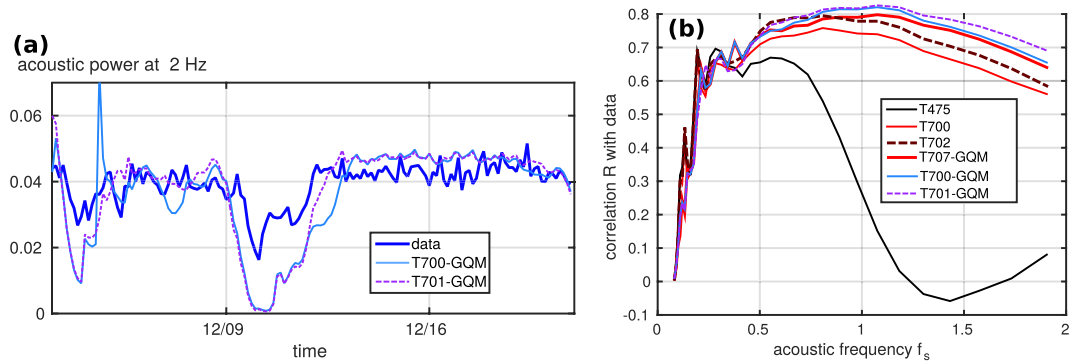

Figure 8. (a) Correlation of modeled acoustic noise at the ALOHA observatory, north of Ohahu Hawaii, for the year 2007 using data provided by (Duennebier et al., 2012) and model runs T475, T702, T707-GQM. Two additional model runs were performed to test the impact of the definition of the direction θ_m in Equation (11) T700-GQM uses an energy-weighted mean direction, and T701-GQM is the exact same run with an mean direction weighted by the orbital velocity variance. (b) Shows time series of predicted noise level at 2 Hz for 2 weeks in December 2007, as in Figure 7f.

parameterizations produces spurious peaks on December 4 in both 1 and 2 Hz time series. That day has a rapidly turning wind, and at some point the wind direction is 220° while the mean wave direction (energy-weighted) is around 330°. That mean direction is the same parameter θ_m in Equation (11) that defines the direction around which a strong dissipation is added by the cumulative effect. Two additional model runs were performed to test the impact of the definition of the direction θ_m in Equation (11) T700-GQM uses an energy-weighted mean direction, and T701-GQM is the exact same run with a mean direction weighted by the orbital velocity variance. The time series shown in 8.a demonstrate that the peak in modeled acoustic noise was indeed associated to the large mismatch between the wind direction and the direction θ_m.

Correlations between model output and measured acoustic levels over the full time series are shown in Figure 8b as a function of frequency. We can see the general better performance of a direction θ_m using a stronger weighting by the higher frequency waves (here using orbital velocities instead of surface elevation). Clearly T475 had very little skill for acoustic frequencies above 0.8 Hz (wave frequencies above 0.4 Hz). Parameterizations by Tolman and Chalikov (1996) and Bidlot et al. (2007) were previously shown to be even worse (Ardhuin et al., 2013). T700 is a clear improvement, even more so when the exact non-linear calculation with GQM replaces the DIA parameterization. It would be interesting to explore higher frequencies, but this is beyond the scope of the present paper.

We note that for wave frequencies in the range 0.3–1 Hz, the good correlation between modeled and measured acoustic noise levels (with frequencies 0.6–2 Hz) supports the idea that noise is mostly driven by waves propagating at angles 80° or more relative to the wind direction. Having a significant energy level in those directions requires a much larger time scale of dissipation for these directions compared to the time scale in the mean wave direction allowing the appropriate balance with the nonlinear 4-wave flux of energy to those directions. In the T707-GQM parameterization we have re-introduced an isotropic cumulative term, this helped in getting more accurate wave heights but it degraded the fit to the acoustic data compared to T700. Hence we conclude that if there is any isotropic dissipation effect it should be weaker than the term introduced in T707-GQM.

3.3. Wave Spectra

The influence of the model parameterization on directional wave spectra may be more easily interpreted with the more familiar kind of data obtained from buoys. Although buoy data may not be reliable at frequencies above 0.4 Hz, they provide separate measurements of the energy level and some measure of the directional spreading. We have chosen the CDIP station 166 located next to Station Papa in the North-East Pacific, also known by its WMO code number 46246. This instrument is a Datawell Waverider buoy maintained by Thomson et al. (2013) which generally provides accurate directional properties (O'Reilly et al., 1996).

Here we illustrate the variation of these quantities for one wave event in 2011, with low winds veering from North-westerly to an Easterly directions in the early hours of 27 January, and increasing to 13 m/s (these are uncorrected winds measured at 5 m height) with a steady Easterly direction, as shown in Figure 9a. The resulting

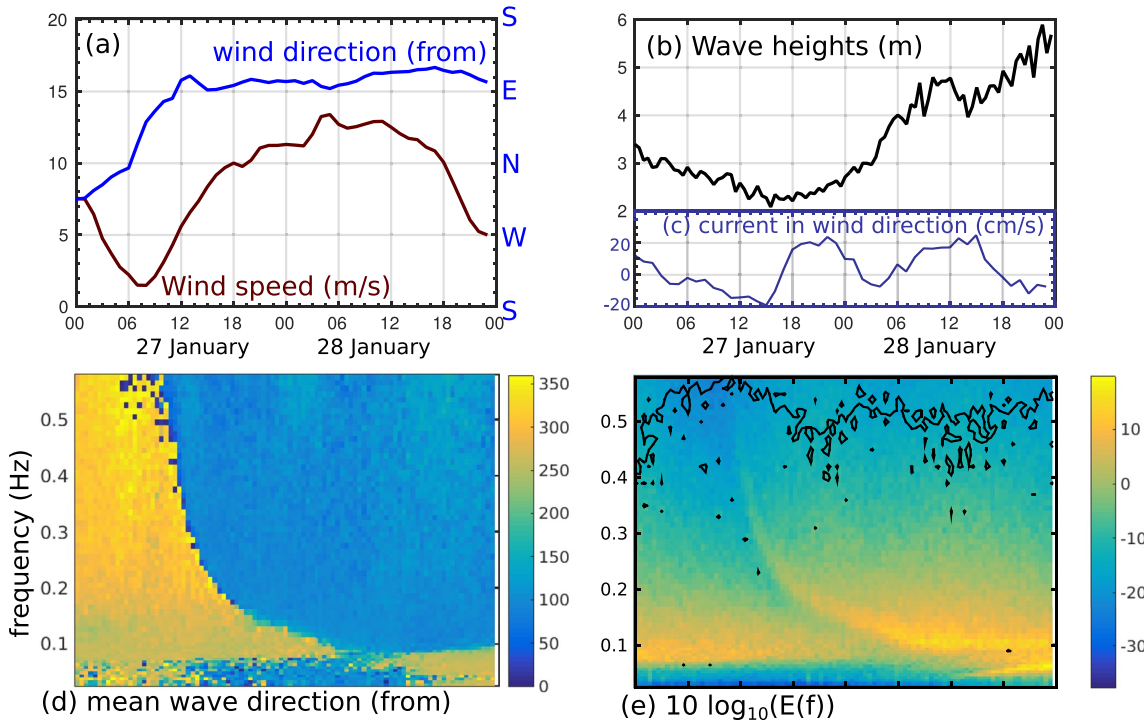

Figure 9. (a) Wind speed, wind direction and (c) significant wave height over a wind event recorded at Ocean Station Papa and nearby buoy 46,246 (CDIP station 166) 27–28 January 2011. (c) Current at 15 m depth projected on the wind direction (d) shows the evolution of the mean wave direction and (e) the evolution of the wave spectrum $E(f)$, with overlaid in black the contour for the check ratio equal to 0.8.

sea state is thus relatively complex on 27 January with the northwesterly waves accounting for most of the wave energy and the easterly windsea progressively growing from high frequencies down to 0.15 Hz. The sea state is a simpler windsea dominated condition on January 28. Model results for different source term settings are shown in Figure 10. We chose to focus on 3 spectral quantities, that are the saturation level of the spectrum, proportional to $f^5E(f)$, the first directional spread $\sigma_1(f)$ and the second directional spread $\sigma_2(f)$ as defined by Kuik et al. (1988) and already discussed in Section 2 and Ewans (1998).

Starting from the saturation levels comes from the idea that we might possibly examine data beyond the equilibrium range in which the energy levels decrease like f^{-4} (Forristall, 1981). As the transition from f^{-4} to f^{-5} is expected to occur at a frequency of the order of $f_n = 0.0225\ g/u_\star$ (Lenain & Melville, 2017), this would be around 2 Hz for a 3 m/s wind and around 0.4 Hz for 14 m/s. In the present event this could be visible in the buoy record on 28 January. Surprisingly the spectral tail shoots up at high frequencies (black lines with dots in Figure 10, panels in top row). The highest values of the measured tail level happen to coincide with times when the current follows the wind with speeds around 20 cm/s, and when the ratio of horizontal to vertical motion (also known as the "check ratio") drops around 0.8 for frequencies above 0.4 Hz. We thus assume that the buoy is somewhat hampered by its mooring and may not be reliable for frequencies above 0.4 Hz. It is nevertheless interesting to examine the behavior of the different model runs. First of all, the energy level in T475 runs is dictated by the imposed f^{-5} tail, which here limit the value of $f^5E(f)$ to about 0.001 $m^2\ Hz^4$, that is, a saturation level of 0.0005 $(2\pi)^4/g^2 = 0.008$, which is rather high. Computations without the imposed tail and using the WRT method for the exact non-linear interactions also produce sharply increasing saturation levels. This anomalous tail level is reduced when using GQM, and the tail can be adjusted to any level when a cumulative breaking term is added in T702 and T707 simulations, based on Equation (8).

Now looking at directional spread σ_1 (middle row in Figure 10) and σ_2 (bottom row), we find that T700 has a tendency to overestimate the directional spread while T700-WRT has a general very good reproduction of the variations of both σ_1 and σ_2. We note that on 28 January, all parameterizations based on Romero (2019) are able to reproduce the monotonic rise in σ_1 toward higher frequencies and a maximum of σ_2 at intermediate frequencies that are typical of an increasing angular lobe separation toward higher frequencies. The T700 calculation in

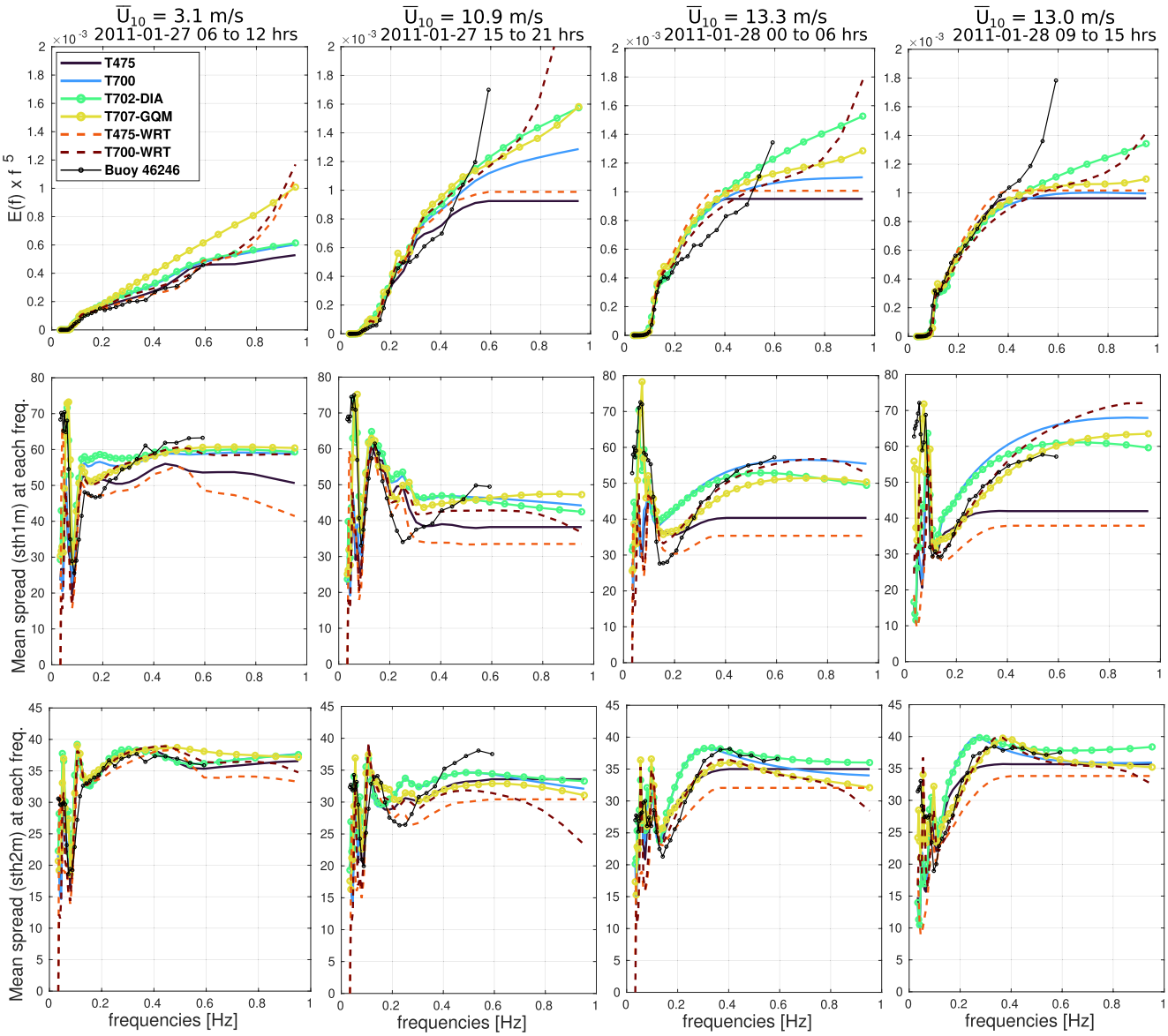

Figure 10. Modeled and measured spectrum, multiplied by f^5 (top panels), first mean spread $\sigma_1(f)$ (middle panels), and second mean spread $\sigma_2(f)$ (bottom panels).

blue has the σ_2 peak at lower frequencies than the buoy data due to the much broader lobes produced by the DIA compared to exact non-linear calculations. We also find that T702 and T707 directional spreads are lower than measured by the buoy, suggesting that our added cumulative term is too strong and that the energy level against the wind direction may be more realistic with the original T700.

4. Discussion and Conclusions

In the previous section, we have looked at the influence of different adjustments of the wave dissipation parameterization T700 by Romero (2019) and compared it to the parameterization T475 by Ardhuin et al. (2010) as modified by Leckler et al. (2013) and adjusted by Alday et al. (2021). The most profound difference introduced by Romero (2019) is a practically "directionally decoupled dissipation": the Λ's are decoupled but the dissipation rates are not. This idea of decoupling was already used to justify the variation in wave energy with wind direction for slanting fetches (Donelan et al., 1985; Pettersson et al., 2010). This parameterization is the first that can give a very weak (close to zero) dissipation rate for waves traveling at 90° from the wind and a strong dissipation rate for waves in the wind direction. This feature is capable of producing directional bimodal spectra, first reported

by Young et al. (1995), with realistic shapes, which was an important objective of Romero (2019). As expected by Romero and Lubana (2022), we have demonstrated that one particular benefit is the capability to reproduce the variability in microseism sources at high frequencies, without compromising the accuracy of wave heights. We have found that most accurate results are obtained with exact non-linear calculations that are now affordable thanks to the Gaussian Quadrature Method (GQM) proposed by Lavrenov (2001), and which we have used extensively. These calculations support the conclusion that the energy level in cross-wind and up-wind directions that is found at frequencies higher than three times the wind sea peak, is the result of a balance between the four-wave interactions and a relatively very weak dissipation, compared to the dissipation in the main wave direction, thereby providing a constraint on this relative strength of the dissipation in different directions.

The different possible adjustments to Romero (2019) that we have proposed were motivated by our curiosity to challenge some of the ad hoc choices that were made, not based on first principles. In particular the choices in the cumulative term of a cosine squared factor and a reference direction in the energy-weighted mean direction θ_m is associated to spurious directional spectral shapes in the presence of swell and in turning wind conditions. A mean direction weighted by orbital-velocity performs better, but one could also try other directions related to the waves that are taken into account in the cumulative term. We have also shown that a wind parameter in the dissipation term is not necessary and $D_W = 0$ in the T702 runs gave satisfactory result. Although wind may directly impact wave breaking at high wind speeds (Soloviev et al., 2014) or in shoaling waves (Feddersen & Veron, 2005) there is no generally established mechanism for such an effect.

Much more questionable is our adjustment of parameters to correct for a low wave height bias. In order to increase wave heights one may increase the wind-wave generation, decrease the dissipation, or even enhance the non-linear four-wave interactions as proposed by Lavrenov (2001) in order to represent fluctuations in the wave field. Ardhuin et al. (2007) have shown that one may use slanting fetch conditions to adjust the magnitude of the input while wave growth with fetch is controlled by the difference between input and dissipation. Another test of the model realism is given by the wind stress, or equivalently the drag coefficient C_d that is the ratio of the friction velocity ($u_\star$) squared and the wind speed squared. We recall that the wind input is generally proportional to $u_\star^2$ and $u_\star$ is a function of the wind input. As a result the feedback of the spectrum tail on wind wave growth via the quasi-linear effect is important (Fabrikant, 1976; Janssen et al., 1992). The difficulty is that $u_\star$ is generally highly dependent on the part of the wave spectrum that is at frequencies higher than highest resolved frequency (in our Case 1 Hz), including the shape of the spectrum in the gravity-capillary range. This aspect of the parameterization was never analyzed with the ST4 parameterizations implemented in WAVEWATCH III. Now that we have removed the forced tail shape from the resolved part of the spectrum, it is interesting to look at the impact on C_d. Figure 11 shows the variability of C_d produced by different source term parameterizations and justifies that future adjustments will be needed, in particular if the wave model is to be used in a coupled ocean-atmosphere context. First of all we note that the viscous part of the wind stress is not included in the default ST4 calculation of $u_\star$, this part gives the shape of the C_d variation for wind speeds under 5 m/s in the COARE3.5 parameterization by Edson et al. (2013). Second, all variants of the ST4 parameterization overestimate C_d for wind speeds 4–15 m/s. This is the result of adjustments of the wind-wave growth parameters to large values in order to reproduce wave heights wen using ERA5 winds. We note that the 707-GQM parameterization (without any imposed tail shape) behaves very much like T475 (with the imposed f^{-5} tail above 2.5 times the mean frequency). T702 gives even higher values of C_d and future adjustment should probably reduce both generation and dissipation terms. For wind speeds over 25 m/s, C_d is artificially reduced by the use of a pre-computed table that limits its value under 0.003. A similar effect is obtained by limiting the value of roughness length in Romero (2019). Although that may be a desirable feature (Donelan et al., 2012), it was not intended as such, and probably does not behave like it should. Another particular aspect that is flawed in the WAVEWATCH III - ST4 implementation of the $u_\star$ calculation is the iteration loop between the source term computation that uses an estimate of $u_\star$ and produces a wave-supported stress τ_w, and the calculation of $u_\star$ that uses τ_w. At present this is limited to 3 iterations and $u_\star$ can be as much as 50% below its converged value: this explains why we used rather high values of the wind-wave growth parameter ($\beta_{\max} = 1.6$ with GQM and $\beta_{\max} = 1.7$ with DIA) compared to WAM model implementations. As a result, correcting these numerical issues and using lower values of $\beta_{\max}$ may lead to more realistic drag coefficients. It remains to be seen how we may use realistic shapes of the spectrum for the unresolved part of the spectrum (Elfouhaily et al., 1997; Yurovskaya et al., 2013) so that the model may produce realistic mean square slopes and drag coefficients in particular for high wind speeds (Janssen & Bidlot, 2023).

The present work was limited by the availability of large datasets with detailed directional wave measurements and reliable measurements of the short wave energy level. In particular we have made no attempt to tune the

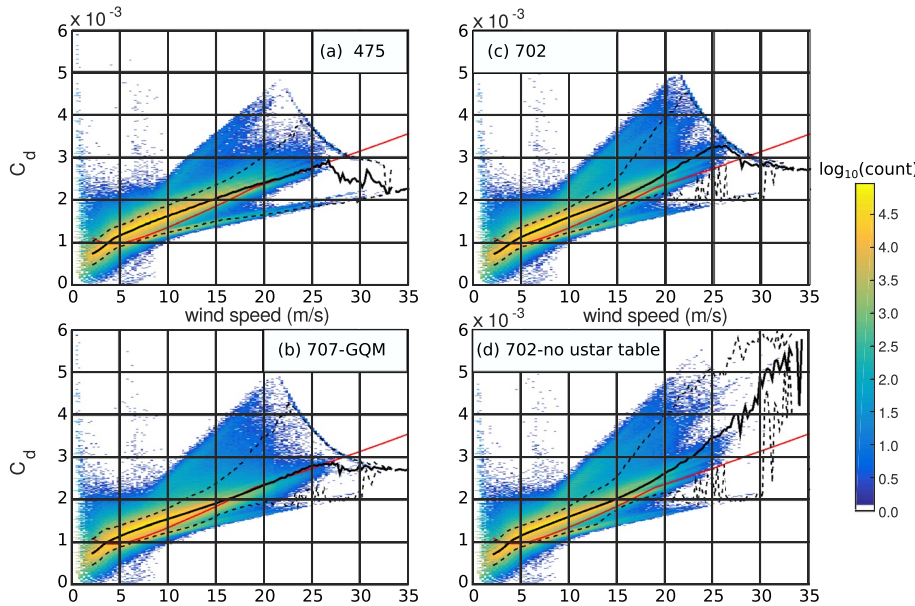

Figure 11. Distribution of drag coefficients for four different model runs over the month of January 2007, taking all model output every 3 h. In each panel the red line is the (Edson et al., 2013) COARE3.5 value of C_d in neutral conditions, the solid black line is the mean value for each wind speed and the dashed lines bracket 95% of the values.

spectral level to an elusive reference and only used stereo-photo and stereo-video measurements as a weak guideline for average wind conditions (Banner et al., 1989; Leckler et al., 2013; Peureux et al., 2018). The tail level may vary widely depending on the choice of cumulative terms. However, if the cumulative term include a significant near-isotropic contribution as given by Equation (7) or (8) it will reduce the directional spread to a level that is lower than observed. We expect that video data in a wider range of conditions (including non-bimodal cases), and also drifting buoy data that may be able to accurately resolve shorter waves, will be key in the detail examination of source term behavior in a wider range of conditions, including turning winds. These data will be very useful for further validation of the direction-integrated energy level at different frequencies.

Clearly much more work is needed on understanding the possible physical processes that may justify the detailed parameterization choices of Romero (2019) or any future evolution on it, and in particular much more research is required to understand the "cumulative effect." Without this understanding, we are left to grope in the dark. As we have shown we can constrain plausible parameterizations of source terms using both directional spreads σ_1 and σ_2 from buoy data, as done by Ewans (1998), up to 0.4–0.6 Hz, and underwater acoustic data for a wider range of frequencies. Further constraints on spectral shapes and source terms can be given by HF and VHF radars (Kirincich, 2016; Tyler et al., 1974) up to 0.5 Hz, and microwave radar backscatter for waves with frequencies from 2 Hz (with L-band radar) to 40 Hz (with Ka-band radars) (Kudryavtsev et al., 2003; Ryabkova et al., 2019). Following Phillips (1984) and Romero (2019), one will probably have to distinguish homogeneous conditions from more complex situations, including current gradients.

Data Availability Statement

In agreement with Fred Duennebier's family and colleagues the bottom pressure spectral data is available at https://doi.org/10.17882/92104. The CDIP wave buoy data are available at cdip.ucsd.edu, ERA5 reanalysis available from https://cds.climate.copernicus.eu and altimeter data from the CNES/NASA/Eumetsat/NOAA mission Jason-2, reprocessed by ESA and available at dx.doi.org/10.5285/8cb46a5efaa74032bf1833438f499cc3. The WAVEWATCH III ® model (The WAVEWATCH III Development Group, 2019) can be downloaded from https://github.com/NOAA-EMC/WW3. The particular modifications used here for ST4 and GQM are available at https://github.com/umr-lops/WW3/tree/GQM_with specific example test cases in regtest/ww3_ts1/input_10ms.

Acknowledgments
We thank CNES for supporting this work as part of the preparation effort for several Earth Observation satellite missions including SWOT, SKIM, and ODYSEA. We are forever indebted to the late Fred Duennebier for providing ocean bottom pressure spectra. The GQM code was kindly provided by Michel Benoit in the TOMAWAC model and first adapted to WAVEWATCH III by Mostafa Beyramzadeh. Other datasets used in the present paper include in situ data from the PAPA Ocean Station provided by the OCS Project Office of NOAA/PMEL, wind time series from WHOTS, WHOI-Hawaii Ocean Time-series Site (WHOTS) mooring, which is supported in part by the National Oceanic and Atmospheric Administration (NOAA) Global Ocean Monitoring and Observing (GOMO) Program through the Cooperative Institute for the North Atlantic Region (CINAR) under Cooperative Agreement NA14OAR4320158. NOAA CPO FundRef number 100007298 to the Woods Hole Oceanographic Institution, and by National Science Foundation Grants OCE-0327513, OCE-0752606, OCE-0926766, OCE-1260164, and OCE-1756517 to the University of Hawaii for the Hawaii Ocean Time-series. We thank Paolo Pezzuto, Leonel Romero and two anonymous reviewers for very constructive comments.

References

Abramovici, F. (1968). Diagnostic diagrams and transfer functions for oceanic wave-guides. *Bulletin of the Seismological Society of America*, *58*(1), 426–456. https://doi.org/10.1785/bssa0580010427

Alday, M., Accensi, M., Ardhuin, F., & Dodet, G. (2021). A global wave parameter database for geophysical applications. part 3: Improved forcing and spectral resolution. *Ocean Modelling*, *166*, 101848. https://doi.org/10.1016/j.ocemod.2021.101848

Ardhuin, F., Chapron, B., & Collard, F. (2009). Observation of swell dissipation across oceans. *Geophysical Research Letters*, *36*(6), L06607. https://doi.org/10.1029/2008GL037030

Ardhuin, F., Gualtieri, L., & Stutzmann, E. (2019). Physics of ambient noise generation by ocean waves. In N. Nakata, L. Gualtieri, & A. Fichtner (Eds.), *Ambient seismic noise* (pp. 69–107). Cambridge University Press.

Ardhuin, F., Herbers, T. H. C., Watts, K. P., van Vledder, G. P., Jensen, R., & Graber, H. (2007). Swell and slanting fetch effects on wind wave growth. *Journal of Physical Oceanography*, *37*(4), 908–931. https://doi.org/10.1175/JPO3039.1

Ardhuin, F., & Jenkins, A. D. (2006). On the interaction of surface waves and upper ocean turbulence. *Journal of Physical Oceanography*, *36*(3), 551–557. https://doi.org/10.1175/JPO2862.1

Ardhuin, F., Lavanant, T., Obrebski, M., Marié, L., Royer, J.-Y., d'Eu, J.-F., et al. (2013). A numerical model for ocean ultra low frequency noise: Wave-generated acoustic-gravity and Rayleigh modes. *The Journal of the Acoustical Society of America*, *134*(4), 3242–3259. https://doi.org/10.1121/1.4818840

Ardhuin, F., Rogers, E., Babanin, A., Filipot, J.-F., Magne, R., Roland, A., et al. (2010). Semi-empirical dissipation source functions for wind-wave models: Part I, definition, calibration and validation. *Journal of Physical Oceanography*, *40*(9), 1917–1941. https://doi.org/10.1175/2010JPO4324.1

Ardhuin, F., Stopa, J. E., Chapron, B., Collard, F., Husson, R., Jensen, R. E., et al. (2019). Observing sea states. *Frontiers in Marine Science*, *6*, 124. https://doi.org/10.3389/fmars.2019.00124

Babanin, A. V., & Young, I. R. (2005). Two-phase behaviour of the spectral dissipation of wind waves. In *Proceedings of the 5th International Symposium Ocean Wave Measurement and Analysis* (Paper Number 51).

Banner, M. L. (1990). Equilibrium spectra of wind waves. *Journal of Physical Oceanography*, *20*(7), 966–984. Retrieved from http://ams.allenpress.com/archive/1520-0485/20/7/pdf/i1520-0485-20-7-966.pdf

Banner, M. L., Babanin, A. V., & Young, I. R. (2000). Breaking probability for dominant waves on the sea surface. *Journal of Physical Oceanography*, *30*(12), 3145–3160. https://doi.org/10.1175/1520-0485(2000)030(3145:BPFDWO)2.0.CO;2

Banner, M. L., Gemmrich, J. R., & Farmer, D. M. (2002). Multiscale measurement of ocean wave breaking probability. *Journal of Physical Oceanography*, *32*(12), 3364–3374. Retrieved from http://ams.allenpress.com/archive/1520-0485/32/12/pdf/i1520-0485-32-12-3364.pdf

Banner, M. L., Jones, I. S. F., & Trinder, J. C. (1989). Wavenumber spectra of short gravity waves. *Journal of Fluid Mechanics*, *198*(-1), 321–344. https://doi.org/10.1017/s0022112089000157

Banner, M. L., & Young, I. R. (1994). Modeling spectral dissipation in the evolution of wind waves. Part I: Assessment of existing model performance. *Journal of Physical Oceanography*, *24*(7), 1550–1570. Retrieved from http://ams.allenpress.com/archive/1520-0485/24/7/pdf/i1520-0485-24-7-1550.pdf

Belmonte Rivas, M., & Stoffelen, A. (2019). Characterizing ERA-Interim and ERA5 surface wind biases using ASCAT. *Ocean Science*, *15*(3), 831–852. https://doi.org/10.5194/os-15-831-2019

Beyramzadeh, M., & Siadatmousavi, S. M. (2022). Skill assessment of different quadruplet wave-wave interaction formulations in the wavewatch-iii model with application to the gulf of Mexico. *Applied Ocean Research*, *127*, 103316. https://doi.org/10.1016/j.apor.2022.103316

Bidlot, J., Janssen, P. A. E. M., & Abdalla, S. (2007). *A revised formulation of ocean wave dissipation and its model impact*. (Technical Report Memorandum 509). ECMWF.

Brekhovskikh, L. M., Goncharov, V. V., Kurtepov, V. M., & Naugolnykh, K. A. (1973). The radiation of infrasound into the atmosphere by surface waves in the ocean. *Izvestiya, Atmospheric and Oceanic Physics*, *9*, 899–907. (In the English translation, 511-515.).

Cox, C., & Munk, W. (1954). Measurement of the roughness of the sea surface from photographs of the sun's glitter. *Journal of the Optical Society of America*, *44*(11), 838–850. https://doi.org/10.1364/josa.44.000838

Cox, C. S., & Jacobs, D. C. (1989). Cartesian diver observations of double frequency pressure fluctuations in the upper levels of the ocean. *Geophysical Research Letters*, *16*(8), 807–810. https://doi.org/10.1029/gl016i008p00807

Crombie, D. D., Hasselmann, K., & Sell, W. (1978). High-frequency radar observations of sea waves travelling in opposition to the wind. *Boundary-Layer Meteorology*, *13*(1–4), 45–54. https://doi.org/10.1007/bf00913861

De Carlo, M., Ardhuin, F., & Pichon, A. L. (2020). Atmospheric infrasound radiation from ocean waves in finite depth: A unified generation theory and application to radiation patterns. *Geophysical Journal International*, *221*, 569–585. https://doi.org/10.1093/gji/ggaa015

Dodet, G., Abdalla, S., Alday, M., Accensi, M., Bidlot, J., & Ardhuin, F. (2022). Error characterization of significant wave heights in multidecadal satellite altimeter product, model hindcast, and in situ measurements using the triple collocation technique. [Dataset]. Journal of Atmospheric and Oceanic Technology, *39*(7), 887–901. https://doi.org/10.1175/JTECH-D-21-0179.1

Donelan, M. A. (2001). A nonlinear dissipation function due to wave breaking. In *Proceedings of ECMWF Workshop on Ocean Wave Forecasting, 2–4 July*. (pp. 87–94).

Donelan, M. A., Curcic, M., Chen, S. S., & Magnusson, A. K. (2012). Modeling waves and wind stress. *Journal of Geophysical Research*, *117*(C11), C00J23. https://doi.org/10.1029/2011JC007787

Donelan, M. A., Hamilton, J., & Hui, W. H. (1985). Directional spectra of wind-generated waves. *Philosophical Transactions of the Royal Society of London A*, *315*, 509–562.

Duennebier, F. K., Lukas, R., Nosal, E.-M., Aucan, J., & Weller, R. A. (2012). Wind, waves, and acoustic background levels at station ALOHA. [Dataset]. Journal of Geophysical Research, *117*(C3), C03017. https://doi.org/10.1029/2011JC007267

Dulov, V. A., & Kosnik, M. V. (2009). Effects of three-wave interactions in the gravity-capillary range of wind waves. *Izvestiya, Atmospheric and Oceanic Physics*, *45*(3), 380–391. https://doi.org/10.1134/s0001433809030116

ECMWF. (2019). *IFS Documentation CY46R1, Part VII: ECMWF wave model*. (Technical Report 333) (p. 103). Author. Retrieved from https://www.ecmwf.int/node/19311

Edson, J. B., Jampana, V., Weller, R. A., Bigorre, S. P., Plueddemann, A. J., Fairall, C. W., et al. (2013). On the exchange of momentum over the open ocean. *Journal of Physical Oceanography*, *43*(8), 1589–1610. https://doi.org/10.1175/JPO-D-12-0173.1

Elfouhaily, T., Chapron, B., Katsaros, K., & Vandemark, D. (1997). A unified directional spectrum for long and short wind-driven waves. *Journal of Geophysical Research*, *102*(C7), 15781–15796. https://doi.org/10.1029/97jc00467

Ewans, K. C. (1998). Observations of the directional spectrum of fetch-limited waves. *Journal of Physical Oceanography*, *28*(3), 495–512. Retrieved from http://ams.allenpress.com/archive/1520-0485/28/3/pdf/i1520-0485-28-4-495.pdf

Fabrikant, A. L. (1976). Quasilinear theory of wind-wave generation. *Izvestiya, Atmospheric and Oceanic Physics*, *12*, 524–526.
Farrell, W. E., & Munk, W. (2008). What do deep sea pressure fluctuations tell about short surface waves? *Geophysical Research Letters*, *35*(7), L19605. https://doi.org/10.1029/2008GL035008
Farrell, W. E., & Munk, W. (2010). Booms and busts in the deep. *Journal of Physical Oceanography*, *40*(9), 2159–2169. https://doi.org/10.1175/2010jpo4440.1
Farrell, W. E., & Munk, W. (2013). Surface gravity waves and their acoustic signatures, 1-30 hz, on the mid-Pacific sea floor. *Journal of the Acoustical Society of America*, *134*(4), 3161–3173. https://doi.org/10.1121/1.4818780
Feddersen, F., & Veron, F. (2005). Wind effects on shoaling wave shape. *Journal of Physical Oceanography*, *35*(7), 1223–1228. https://doi.org/10.1175/jpo2753.1
Forristall, G. Z. (1981). Measurements of a saturated range in ocean wave spectra. *Journal of Geophysical Research*, *86*(C9), 8075–8084. https://doi.org/10.1029/jc086ic09p08075
Gagnaire-Renou, E. (2010). *Amelioration de la modelisation spectrale des etats de mer par un calcul quasi-exact des interactions non-lineaires vague-vague (Unpublished doctoral dissertation)*. Université du Sud Toulon Var.
Gagnaire-Renou, E., Benoit, M., & Forget, P. (2010). Ocean wave spectrum properties as derived from quasi-exact computations of nonlinear wave-wave interactions. *Journal of Geophysical Research*, *115*(C12), C12058. https://doi.org/10.1029/2009JC005665
Guimarães, P. V., Ardhuin, F., Bergamasco, F., Leckler, F., Filipot, J.-F., Shim, J.-S., et al. (2020). A data set of sea surface stereo images to resolve space-time wave fields. *Scientific Data*, *7*(1), 145. https://doi.org/10.1038/s41597-020-0492-95
Hanafin, J., Quilfen, Y., Ardhuin, F., Sienkiewicz, J., Queffeulou, P., Obrebski, M., et al. (2012). Phenomenal sea states and swell radiation: A comprehensive analysis of the 12-16 February 2011 North Atlantic storms. *Bulletin of the American Meteorological Society*, *93*(12), 1825–1832. https://doi.org/10.1175/BAMS-D-11-00128.1
Hasselmann, K. (1962). On the non-linear energy transfer in a gravity wave spectrum, part 1: General theory. *Journal of Fluid Mechanics*, *12*(04), 481–501. https://doi.org/10.1017/s0022112062000373
Hasselmann, K. (1963). A statistical analysis of the generation of microseisms. *Reviews of Geophysics*, *1*(2), 177–210. https://doi.org/10.1029/rg001i002p00177
Hasselmann, K., Raney, R. K., Plant, W. J., Alpers, W., Shuchman, R. A., Lyzenga, D. R., et al. (1985). Theory of synthetic aperture radar ocean imaging: A MARSEN view. *Journal of Geophysical Research*, *90*(C3), 4659–4686. https://doi.org/10.1029/jc090ic03p04659
Hersbach, H., Bell, B., Berrisford, P., Hirahara, S., Horányi, A., Muñoz-Sabater, J., et al. (2020). The ERA5 global reanalysis. *Quarterly Journal of the Royal Meteorological Society*, *146*(730), 1999–2049. https://doi.org/10.1002/qj.3803
Hoeke, R. K., McInnesa, K. L., Kruger, J. C., McNaught, R. J., Hunter, J. R., & Smithers, S. G. (2013). Widespread inundation of Pacific islands triggered by distant-source wind-waves. *Global and Planetary Change*, *108*, 128–138. https://doi.org/10.1016/j.gloplacha.2013.06.006
Janssen, P. A. E. M. (1991). Quasi-linear theory of wind wave generation applied to wave forecasting. *Journal of Physical Oceanography*, *21*(11), 1631–1642. Retrieved from http://journals.ametsoc.org/doi/pdf/10.1175/1520-0485%281991%29021%3C1631%3AQLTOWW%3E2.0.CO%3B2
Janssen, P. A. E. M., & Bidlot, J.-R. (2023). Wind–wave interaction for strong winds. *Journal of Physical Oceanography*, *53*(3), 779–804. https://doi.org/10.1175/JPO-D-21-0293.1
Janssen, P. A. E. M., Lionello, P., Feistad, M., & Hollingsworth, A. (1992). Hindcasts and data assimilation studies with the WAM model during the Seasat period. *Journal of Geophysical Research*, *94*(C1), 973–993. https://doi.org/10.1029/jc094ic01p00973
Kantha, L. (2006). A note on the decay rate of swell. *Ocean Modelling*, *11*(1–2), 167–173. https://doi.org/10.1016/j.ocemod.2004.12.003
Kirincich, A. (2016). Remote sensing of the surface wind field over the coastal ocean via direct calibration of HF radar backscatter power. *Journal of Atmospheric and Oceanic Technology*, *33*(7), 1377–1392. https://doi.org/10.1175//JTECH-D-15-0242.1
Komen, G. J., Cavaleri, L., Donelan, M., Hasselmann, K., Hasselmann, S., & Janssen, P. A. E. M. (1994). *Dynamics and modelling of ocean waves*. Cambridge University Press.
Kudryavtsev, V., Hauser, D., Caudal, G., & Chapron, B. (2003). A semiempirical model of the normalized radar cross-section of the sea surface 2. Radar modulation transfer function. *Journal of Geophysical Research*, *108*(C3), 8055. https://doi.org/10.1029/2001JCOO1004
Kuik, A. J., van Vledder, G. P., & Holthuijsen, L. H. (1988). A method for the routine analysis of pitch-and-roll buoy wave data. *Journal of Physical Oceanography*, *18*(7), 1020–1034. Retrieved from http://journals.ametsoc.org/doi/pdf/10.1175/1520-0485%281987%29017%3C0845%3ATROWDT%3E2.0.CO%3B2
Lavrenov, I. V. (2001). Effect of wind wave parameter fluctuation on the nonlinear spectrum evolution. *Journal of Physical Oceanography*, *31*(4), 861–873. https://doi.org/10.1175/1520-0485(2001)031<0861:eowwpf>2.0.co;2
Lavrenov, I. V., & Ocampo-Torres, F. J. (1999). Angular distribution effect on eakly nonlinear energy transfer in the spectrum of wind waves. *Izvestiya, Atmospheric and Oceanic Physics*, *35*, 278–290.
Leckler, F., Ardhuin, F., Filipot, J.-F., & Mironov, A. (2013). Dissipation source terms and whitecap statistics. *Ocean Modelling*, *70*(9), 62–74. https://doi.org/10.1016/j.ocemod.2013.03.007
Leckler, F., Ardhuin, F., Peureux, C., Benetazzo, A., Bergamasco, F., & Dulov, V. (2015). Analysis and interpretation of frequency-wavenumber spectra of young wind waves. *Journal of Physical Oceanography*, *45*(10), 2484–2496. https://doi.org/10.1175/JPO-D-14-0237.1
Lenain, L., & Melville, W. K. (2017). Measurements of the directional spectrum across the equilibrium saturation ranges of wind-generated surface waves. *Journal of Physical Oceanography*, *47*(8), 2123–2138. https://doi.org/10.1175/jpo-d-17-0017.1
Long, C. E., & Resio, D. T. (2007). Wind wave spectral observations in Currituck Sound, North Carolina. *Journal of Geophysical Research*, *112*(C5), C05001. https://doi.org/10.1029/2006JC003835
Longuet-Higgins, M. S. (1950). A theory of the origin of microseisms. *Philosophical Transactions of the Royal Society of London A*, *243*, 1–35.
Longuet-Higgins, M. S., Cartwright, D. E., & Smith, N. D. (1963). Observations of the directional spectrum of sea waves using the motions of a floating buoy. In *Ocean wave spectra, proceedings of a conference* (pp. 111–136). Prentice-Hall.
Mentaschi, L., Besio, G., Cassola, F., & Mazzino, A. (2013). Problems in RMSE-based wave model validations. *Ocean Modelling*, *72*, 53–58. https://doi.org/10.1016/j.ocemod.2013.08.003
Miles, J. W. (1957). On the generation of surface waves by shear flows. *Journal of Fluid Mechanics*, *3*(02), 185–204. https://doi.org/10.1017/s0022112057000567
O'Reilly, W. C., Herbers, T. H. C., Seymour, R. J., & Guza, R. T. (1996). A comparison of directional buoy and fixed platform measurements of Pacific swell. *Journal of Atmospheric and Oceanic Technology*, *13*(1), 231–238. https://doi.org/10.1175/1520-0426(1996)013<0231:acodba>2.0.co;2
Perignon, Y., Ardhuin, F., Cathelain, M., & Robert, M. (2014). Swell dissipation by induced atmospheric shear stress. *Journal of Geophysical Research*, *119*(10), 6622–6630. https://doi.org/10.1002/2014JC009896

Pettersson, H., Kahma, K. K., & Tuomi, L. (2010). Wave directions in a narrow bay. *Journal of Physical Oceanography*, *40*(1), 155–169. Retrieved from http://journals.ametsoc.org/doi/pdf/10.1175/2009JPO4220.1

Peureux, C., & Ardhuin, F. (2016). Ocean bottom pressure records from the cascadia array and short surface gravity waves. *Journal of Geophysical Research*, *121*(5), 2862–2873. https://doi.org/10.1002/2015JC011580

Peureux, C., Ardhuin, F., & Guimaraes, P. V. (2021). On the unsteady steepening of short gravity waves near the crests of longer waves in the absence of generation or dissipation. *Journal of Geophysical Research*, *126*(1). https://doi.org/10.1029/2020JC016735

Peureux, C., Benetazzo, A., & Ardhuin, F. (2018). Note on the directional properties of meter-scale gravity waves. *Ocean Science*, *14*(1), 41–52. https://doi.org/10.5194/os-14-41-2018

Phillips, O. M. (1958). The equilibrium range in the spectrum of wind-generated waves. *Journal of Fluid Mechanics*, *4*(04), 426–433. https://doi.org/10.1017/s0022112058000550

Phillips, O. M. (1984). On the response of short ocean wave components at a fixed wavenumber to ocean current variations. *Journal of Physical Oceanography*, *14*(9), 1425–1433. https://doi.org/10.1175/1520-0485(1984)014⟨1425:OTROSO⟩2.0.CO;2

Phillips, O. M. (1985). Spectral and statistical properties of the equilibrium range in wind-generated gravity waves. *Journal of Fluid Mechanics*, *156*(-1), 505–531. https://doi.org/10.1017/s0022112085002221

Rogers, W. E., Babanin, A. V., & Wang, D. W. (2010). Observation-consistent input and whitecapping dissipation in a model for wind-generated surface waves: Description and simple calculations. *Journal of Atmospheric and Oceanic Technology*, *29*(9), 1329–1346. https://doi.org/10.1175/jtech-d-11-00092.1

Romero, L. (2019). Distribution of surface wave breaking fronts. *Geophysical Research Letters*, *46*(17–18), 10463–10474. https://doi.org/10.1029/2019GL083408

Romero, L., & Lubana, K. (2022). On the bimodality of the wind-wave spectrum: Mean-squared-slopes and azimuthal overlap integral. *Journal of Physical Oceanography*, *52*(7), 1549–1562. https://doi.org/10.1175/JPO-D-21-0299.1

Romero, L., & Melville, K. W. (2010). Airborne observations of fetch-limited waves in the gulf of tehuantepec. *Journal of Physical Oceanography*, *40*(3), 441–465. https://doi.org/10.1175/2009jpo4127.1

Romero, L., Melville, W. K., & Kleiss, J. M. (2012). Spectral energy dissipation due to surface wave breaking. *Journal of Physical Oceanography*, *42*(9), 1421–1444. https://doi.org/10.1175/jpo-d-11-072.1

Ryabkova, M., Karaev, V., Guo, J., & Titchenko, Y. (2019). A review of wavespectrum models as applied to the problem of radar probing of the sea surface. *Journal of Geophysical Research*, *124*(10), 7104–7134. https://doi.org/10.1029/2018JC014804

Soloviev, A. V., Lukas, R., Donelan, M. A., Haus, B. K., & Ginis, I. (2014). The air-sea interface and surface stress under tropical cyclones. *Scientific Reports*, *4*(1), 5306. https://doi.org/10.1038/srep05306

Stopa, J. E., Ardhuin, F., & Girard-Ardhuin, F. (2016). Wave climate in the Arctic 1992-2014: Seasonality and trends. *The Cryosphere*, *10*(4), 1605–1629. https://doi.org/10.5194/tc-10-1605-2016

Sutherland, P., & Melville, W. K. (2013). Field measurements and scaling of ocean surface wave-breaking statistics. *Geophysical Research Letters*, *40*(12), 3074–3079. https://doi.org/10.1002/grl.50584

Sutherland, P., & Melville, W. K. (2015). Field measurements of surface and near-surface turbulence in the presence of breaking waves. *Journal of Physical Oceanography*, *45*(4), 943–965. https://doi.org/10.1175/JPO-D-14-0133.1

Swail, V., Jensen, R., Lee, B., Turton, J., Thomas, J., Gulev, S., et al. (2009). Wave measurements, needs and developments for the next decade. In *Proceedings of oceanObs'09: sustained ocean observations and information for society*, (Vol. 2, pp. 999–1008). European Space Agency. https://doi.org/10.5270/OceanObs09

The WAVEWATCH III® Development Group. (2019). User manual and system documentation of WAVEWATCH III ® version 6.07 [Software] (Technical Note 333). NOAA/NWS/NCEP/MMAB, 465. + Appendices. Retrieved from https://github.com/NOAA-EMC/WW3

Thomson, J., D'Asaro, E. A., Cronin, M. F., Rogers, W. E., Harcourt, R. R., & Shcherbina, A. (2013). Waves and the equilibrium range at ocean weather station P. *Journal of Geophysical Research*, *118*(11), 595–5962. https://doi.org/10.1002/2013JC008837

Tolman, H. L., & Chalikov, D. (1996). Source terms in a third-generation wind wave model. *Journal of Physical Oceanography*, *26*(11), 2497–2518. Retrieved from http://journals.ametsoc.org/doi/pdf/10.1175/1520-0485%281996%29026%3C2497%3ASTIATG%3E2.0.CO%3B2

Tracy, B. A., & Resio, D. T. (1982). *Theory and calculation of the nonlinear energy transfer between sea waves in deep water*. (Technical Report 11). U.S. Army Engineer Waterways Experiment Station.

Tyler, G. L., Teague, C. C., Stewart, R. H., Peterson, A. M., Munk, W. H., & Joy, J. W. (1974). Wave directional spectra from synthetic aperture observations of radio scatter. *Deep-Sea Research*, *21*(12), 989–1016. https://doi.org/10.1016/0011-7471(74)90063-1

van Vledder, G. P. (2006). The WRT method for the computation of non-linear four-wave interactions in discrete spectral wave models. *Coastal Engineering*, *53*(2–3), 223–242. https://doi.org/10.1016/j.coastaleng.2005.10.011

Webb, D. J. (1978). Nonlinear transfer between sea waves. *Deep-Sea Research*, *25*(3), 279–298. https://doi.org/10.1016/0146-6291(78)90593-3

Young, I. R., Verhagen, L. A., & Banner, M. L. (1995). A note on the bimodal directional spreading of fetch-limited wind waves. *Journal of Geophysical Research*, *100*(C1), 773–778. https://doi.org/10.1029/94jc02218

Yurovskaya, M. V., Dulov, V. A., Chapron, B., & Kudryavtsev, V. N. (2013). Directional short wind wave spectra derived from the sea surface photography. *Journal of Geophysical Research*, *113*(9), C12024–C14394. https://doi.org/10.1002/jgrc.20296